

Computational Prediction of Aerodynamic Forces for a Simplified Integrated Tractor-Trailer Geometry

Kambiz Salari¹, Jason M. Ortega², and Paul J. Castellucci³
Lawrence Livermore National Laboratory, Livermore, CA 94551

Simulations are performed on a 1/8th scale simplified tractor/trailer geometry for validating the drag prediction capabilities of selected RANS turbulence models. The drag coefficients, as well as the surface pressures and flow structures, are compared to experimental data obtained from the NASA Ames 7'x10' wind tunnel at 0° and 10° yaw. Among the turbulence models, the two-equation models reasonably predict the drag coefficient. While both the one- and two-equation models reproduce the overall experimental flow features, they do not properly depict the correct details of the separated flows.

Nomenclature

A	= cross-sectional area
C_d	= drag coefficient
C_l	= lift coefficient
C_p	= pressure coefficient
C_s	= side force coefficient
M	= Mach number
P_s	= static pressure
P_{sw}	= wall reference pressure
P_t	= total pressure
q_∞	= dynamic pressure
Re_w	= trailer width-based Reynolds number
T_s	= static temperature
T_t	= total temperature
V_{ts}	= test-section velocity
w	= trailer width
x, y, z	= tunnel coordinates
y^+	= surface normal coordinate in wall units
ρ	= air density
Ψ	= yaw angle

¹ Staff Scientist, Computational Physics Group / NTED, P.O. Box 808, L-644, and Associate Fellow.

² Staff Scientist, Computational Physics Group / NTED, P.O. Box 808, L-644, and Member.

³ Student, Institute for Scientific Computing Research, P.O. Box 808, L-644, and Member.

This work has been authored by a contractor of the U.S. Government under Contract No. W-7405-ENG-48 between the United States Department of Energy and The Regents of the University of California for the operation of LLNL. Accordingly, the U.S. Government retains a non-exclusive royalty-free license to publish or reproduce the published form of the Contribution, or allow others to do so for U.S. Government purposes. UCRL-CONF-204887

I. Introduction

A typical class 8 tractor-trailer traveling at highway speed requires approximately 65% of the total energy produced by the engine to overcome aerodynamic drag. It is estimated that reducing the drag coefficient of a heavy vehicle by 25% would result in a total U.S. yearly savings of roughly 2 billion gallons of diesel fuel.¹ In 1996, the U.S. Department of Energy Office of Heavy Vehicle Technologies (OHVT) recognized this potential benefit and founded a research and development effort to reduce the aerodynamic drag/emissions of heavy vehicles. The purpose of this effort is to identify and to establish through use of experiments and computational simulations the dominant flow structures around heavy vehicles that are significant contributors to the total aerodynamic drag. Such flow structures are known to exist in the gap between the tractor and trailer, the vehicle underbody, and the base of the trailer.² With the knowledge gained from this effort, drag reducing devices can then be designed to mitigate the effects of these flow structures, thereby reducing the aerodynamic drag of tractor-trailers.

This DOE research project is investigating the applicability of state-of-the-art computational modeling and simulations to predict the flow field surrounding bluff bodies. This serves to provide expertise in applying flow modeling tools in the aerodynamic design process of heavy vehicles. Contributors to this program include seven organizations: Argonne National Laboratory (ANL), California Institute of Technology (Caltech), Georgia Tech Research Institute (GTRI), Lawrence Livermore National Laboratory (LLNL), National Aeronautics and Space Administration (NASA), Sandia National Laboratories (SNL), and University of Southern California (USC).

Traditionally, heavy vehicle aerodynamicists have relied upon experimental data from wind tunnels and road tests for design purposes. However, computer simulations of aerodynamic flow around heavy vehicles have significantly matured over the past five years. Thus, heavy vehicle manufacturers are beginning to integrate this new capability into their vehicle aerodynamic design process. LLNL's responsibility in this effort is to provide heavy vehicle manufacturers with guidance on computational modeling and simulations, advanced numerical schemes, grid generation, turbulence modeling, solution accuracy, and aero-devices for drag reduction. The truck industry depends heavily on steady Reynolds-Averaged Navier-Stokes (RANS) computations to study the drag of heavy vehicles. This investigation will highlight the strengths and the weaknesses of RANS in predicting the flow field and the resulting aerodynamic forces for a simplified heavy vehicle. We conduct steady computations using RANS on a generic tractor-trailer type geometry known as the Ground Transportation System (GTS) designed by Sandia National Laboratories. Gutierrez et al.³ give an overview of the Ground Transportation System project and provide the details of the GTS geometry. The GTS was tested in the Texas A&M University 7'x10' wind tunnel in 1995 (Ref. 4) and in the NASA Ames 7'x10' wind tunnel in 1999 (Ref. 5). Computational flow simulations have also been performed on the GTS.⁶⁻⁸

The layout of the remainder of the paper is as follows. A brief explanation of the NASA Ames experiment that was used to validate the computational results is described in Section 2. Sections 3 through 7 describe the computational boundary conditions, tools, turbulence model selection, mesh generation, and numerical algorithm used for the GTS simulations. The computational results are presented in Section 9. Conclusions follow in Section 10.

II. NASA Ames Wind Tunnel Experiment

The 1/8th scale GTS model was studied experimentally in the NASA Ames 7'x10' wind tunnel in 1999.⁵ Experimental measurements were made of aerodynamic forces, surface pressures, surface skin friction (oil film interferometry), and 3-D velocity fields (particle image velocimetry, PIV). Figure 1 shows the GTS model installation in the NASA Ames 7'x10' wind tunnel. The GTS model is instrumented with a total of 79 surface pressure taps as shown in Fig. 2. An additional 60 surface pressure taps are positioned on the tunnel wall as shown in Fig. 3. Among the wall surface pressure taps a reference location is chosen to be used in calculation of the pressure coefficients. A tabular list of the tap locations is available from Storms et al.⁵

The surface pressure coefficient, C_p , is computed using the wall reference pressure, p_{sw} , and the tunnel dynamic pressure, q_∞ , from

$$C_p = \frac{P - P_{sw}}{q_\infty} \quad (1)$$

where q_∞ is computed from the difference between the settling-chamber static pressure, p_t , and the reference tap wall pressure.

Instantaneous and time-averaged flow field in the trailer wake are measured using three-component PIV for several laser sheet orientations as shown in Table 1. The coordinates in this table are non-dimensionalized by the trailer width, $w = 12.75$ in (32.38 cm). The empty tunnel test-section turbulence intensity is 0.25% at a Mach number, M , of 0.22. The uncertainties in the measured and computed parameters are as follows: $\pm 0.1^\circ$ for the yaw angle; ± 0.01 for the aerodynamic force coefficients; ± 0.004 for the computed pressure coefficients; $\pm 2\%$ for in-plane PIV velocities; and $\pm 4\%$ for out-of-plane PIV velocities.

III. Wind Tunnel Modeling

To accurately model the flow conditions in the tunnel test-section, a portion of the NASA Ames 7'x10' wind tunnel is modeled. Careful attention is paid to matching the simulation boundary conditions to the wind tunnel conditions. Since the GTS model was mounted on the tunnel floor and exposed to the floor boundary layer, the accuracy of a computational prediction depends on how well the upstream boundary layer profile is represented. To capture the proper boundary layer profile and mass flow rate at the test-section entrance, the inflow boundary must be positioned sufficiently far upstream from the test-section. The outflow boundary is positioned downstream of the test-section in the diffuser to prevent interference with the trailer wake flow structure. The initial computational domain (Fig. 4a) contained the settling chamber, contraction, test-section and part of expansion of the 7'x10' wind tunnel. However, after several computations, it was decided that a truncated wind tunnel model (Fig. 4b) was sufficient to accurately represent the flow in the test-section, including the incoming boundary layer. Modeling a portion of the wind tunnel allows use of:

- wind tunnel data not corrected for model blockage
- the experimental reference pressure location in the calculation of pressure coefficients
- the experimental boundary layer measurements

The truncated wind tunnel geometry is used for all subsequent simulations. Since the model is significantly far from the top and side walls, they are modeled as slip boundaries, while the tunnel floor is modeled as a no-slip boundary. For the inflow boundary, the total conditions (pressure and temperature) are held constant and the velocity field is allowed to develop. For the outflow boundary, a static pressure is defined. Some of the required parameters for inflow and outflow boundaries are not available from the experiment and need to be evaluated. Details on how to obtain these parameters are provided in Section 8.

IV. Computational Tools and Post-processing

NASA OVERFLOW v2.0s, a fully compressible, 3-D, finite volume code employing overset grids, is used for all simulations. OVERFLOW solves the compressible Navier-Stokes equations in a non-dimensional form. The pre-processing necessary for solution of overset grids in OVERFLOW is achieved with PEGASUS v5. This code prepares volume grids for the flow solver by computing interpolation stencils and removing grid points contained inside solid bodies. Forces and moments on the overset surface grids are computed by FOMOCO, part of the CHIMERA Tool Set. Interactive Data Language (IDL), Ensign (Computational Engineering International), and Tecplot (Amtec Engineering Inc.) are used in post-processing and feature extraction.

V. Turbulence Model Selection

One of the goals of the DOE research initiative is to provide the tractor and the trailer manufacturers with a knowledge base that describes the advantages and disadvantages of widely used turbulence models in predicting heavy vehicle aerodynamics. The following commonly used RANS turbulence models are selected: one-equation Spalart-Allmaras (SA)⁹, two-equation Wilcox $k-\omega$ 1988 version (KW)¹⁰, and two-equation Menter $k-\omega$ models (BSL)¹¹. In all simulations, the flow is assumed to be fully turbulent and no attempt is made to model transition. Additionally, all turbulence equations are integrated to the wall and no wall functions are used. Wall function usage is prevalent in commercial codes and can potentially reduce the number of elements needed in the

simulation by 50%. Argonne National Laboratory, as part of the DOE consortium, is currently investigating the influence of wall functions on predicting the flow field around heavy vehicles.

The type of discretization that is applied to the turbulence equations can possibly influence the predictive capability of these models. In most commercial codes, the advective part of these equations is typically discretized using the first-order upwind scheme to ensure robustness. However, this scheme is quite dissipative and can influence the computational results. In this effort, a sensitivity study at 10° yaw was performed on the first- vs. the second-order treatment of the advective part of the turbulence equations.

VI. Mesh Generation

GRIDGEN is used to construct all of the meshes needed for this investigation. For the empty tunnel simulations, two single-block grids (Fig. 5) with 466,240 and 816,000 elements are constructed. For the GTS baseline model in the NASA Ames 7'x10' wind tunnel, two grids for each yaw angle (0° and 10°) are generated. Grid statistics for these meshes are presented in Tables 2 and 3. Figures 6 and 7 show the meshes for the GTS model within the wind tunnel. For all no-slip surfaces, y^+ values of approximately 0.4-0.5 are maintained for all grids. The origin of the mesh coordinate system is located on the tunnel floor at the entrance of the test-section along the symmetry plane, which is different from that given in the NASA TM report⁵ (Fig. 5). All computed results are presented in the mesh coordinate system. All meshes are non-dimensionalized by the GTS trailer width ($w=12.75$ in or 32.38 cm).

VII. Computational Setup

Subsonic GTS computations are run using a low-Mach number preconditioner in OVERFLOW. The ARC3D, 3-factor, diagonal scheme is used with a 4th-order dissipation term that is set to 0.01 for stability. To accelerate convergence toward steady-state, grid sequencing and Jacobian time-step scaling is employed. All computations are performed using 256 processors on a tightly coupled Linux cluster (11.2 TF) with 1,152 nodes, each with two 2.4-GHz Pentium 4 Xeon processors and 4 GB of memory. Typical simulation time is about 24 hours for the medium-sized meshes.

VIII. Tunnel Empty Simulations

Empty tunnel simulations are needed to establish a proper boundary layer profile at the test-section entrance. Run 404 from the NASA experiment⁵ is selected for empty tunnel simulations. The following parameters, at the tunnel pressure ring, are given for this run: total pressure 97984.845 N/m², total temperature 291.827 °K, and static pressure 94558.03 N/m². In the NASA experiment, the boundary layer profile was measured by a boundary layer rake at the origin of the mesh coordinate system. Figure 5 shows the size of the computational domain. The inflow boundary condition maintains the total pressure and temperature by extrapolating the mass flow. The tunnel mass flow is computed at the test section from

$$\dot{m} = \frac{P_t A M \sqrt{\gamma}}{\sqrt{R T_t}} \left(1 + \left(\frac{\gamma - 1}{2} \right) M^2 \right)^{\frac{\gamma + 1}{2 - 2\gamma}} \quad (2)$$

where $A = 6.5032 \text{ m}^2$ is the cross-sectional area of the test-section and M is the average Mach number at the test-section computed by

$$M = \left(\frac{2}{\gamma - 1} \right) \left(\left(\frac{P_t}{P_s} \right)^{\frac{\gamma - 1}{\gamma}} - 1 \right)^{\frac{1}{2}} \quad (3)$$

The test-section Mach number from Eq. 3 is computed to be 0.226. Substituting this value into Eq. 2, we obtain an empty tunnel mass flow rate of 571.26 kg/s. Knowing the mass flow rate and inflow area ($A = 9.2514 \text{ m}^2$), the inflow Mach number is computed from Eq. 2. The solution to Eq. 3 has two real roots. The subsonic solution of

0.156 is selected to be the inflow Mach number. Given this Mach number, the inflow static pressure is computed to be 94,558.03 N/m² and static temperature to be 291.73 °K.

The specified pressure outflow boundary condition requires the ratio of inflow to outflow static pressures. Multiple empty tunnel simulations with varying back pressure are performed to match the Mach number at the test-section mid-height above the center of the turntable to that of the experiments. After five to six iterations, we obtain an outflow pressure ratio of 0.9992, which matches the experimental test-section Mach number to within 0.07%. This back pressure is then held constant for both the coarse and medium mesh calculations.

Figures 8 and 9 present Mach and pressure contours on the tunnel symmetry plane. These figures highlight the uniformity of the velocity and pressure fields in the test-section, as well as the growing boundary layer on the tunnel floor. Figure 10 presents the comparison of the computed boundary layer profile at the test-section entrance to that of the experimental data. All turbulence models perform reasonably well in predicting the correct boundary profile for the test-section. As stated earlier, the shape of this boundary layer profile impacts the accuracy of GTS flow calculations. Figure 11 presents similar calculations with only the BSL model using coarse and medium meshes. The computational and experimental profiles are nearly identical, suggesting a grid-resolved solution for the empty tunnel simulation. In the following sections, the tunnel resolution is increased in the vicinity of the GTS model to capture the separated flow regions on the upper, bottom, and leeward sides of the GTS.

IX. Computational Results

The NASA Ames wind tunnel test provides data for a range of yaw angles from -14° to +14°. Among these yaw angles, 0° and 10° yaw are selected to be studied. The 0° yaw case provides the baseline in which the flow remains attached to the GTS body except over the base of the trailer. However, at 10° yaw, there are multiple separation regions and vortex structures around the GTS body, placing a greater demand on the turbulence models. Since we anticipate the most complex flow structures to be present in the separated regions, the trailer wake is investigated by comparing the computed results to the time-averaged experimental PIV data. The available PIV laser sheets include the streamwise vertical plane at ($y/w=0$) for 0° yaw, the horizontal plane at the trailer mid-height for 0° and 10° yaw, and the cross-stream plane at distances of 0.353 w and 1.137 w from the base of the trailer for 0° and 10° yaw, respectively. Note that the PIV laser sheet coordinate system for the 0° and 10° yaw cases are different. At 0° yaw, the data are presented with a body fixed coordinate system as shown in Fig. 2. At 10° yaw, the coordinate system remains aligned with GTS, but the origin lies ahead and starboard of the model. To highlight the location of the laser sheet, its position is included in relevant particle trace plots. Note that the particle emitters are identical for all of the particle trace plots within a given plane. Due to the low resolution of the experimental velocity field data, the positions of the vortex cores are obtained to within approximately $\pm 0.025w$. In addition, vortex core locations are obtained from the experimental data. In the next section, detailed results for each yaw angle are presented.

A. Results for 0° yaw

From the NASA experiment, run 7 point 9 with the GTS baseline configuration at 0° yaw is selected for simulation.⁵ The following flow conditions are provided for this run: $M = 0.28$, $V_{ts} = 93.91$ m/s, $q_{\infty} = 5314.89$ N/m², $Re_w = 2.08 \times 10^6$, $p_t = 102649.217$ N/m², $T_t = 284.66$ °K, $p_s = 97339.115$ N/m², and $T_s = 280.36$ °K, and $\rho = 1.206$ kg/m³. The coarse and medium mesh statistics are presented in Tables 2 and 3. A tunnel mass flow rate of 714.191 kg/s is computed from the static pressure of 98333.732 N/m² at the tunnel pressure ring using Eqs. 2 and 3. Knowing the mass flow rate and tunnel geometry, the inflow Mach number of 0.1854 is computed from Eq. 3. The inflow boundary condition parameters are $M = 0.1854$, $p_s = 100,214.496$ N/m², $T_s = 282.715$ °K, and inflow $Re_w = 1.42 \times 10^6$. An iterative procedure is used to determine an outflow static pressure of 0.99822, which produces a pressure ring Mach number that is to within 0.08% of the experimental value. Table 4 summarizes the simulations that are performed at 0° yaw.

The medium mesh result using the full Menter SST turbulence model simulation produces a non-physical separation region on the front corner of the GTS. This separated region is unaffected by grid sequencing and mesh resolution. The shear stress limiter of the BSL model was identified as a possible cause of the separation and was deactivated within OVERFLOW. The resulting simulations show no sign of this separation region. Hence, for all presented results, the Menter $k-\omega$ turbulence model is used with no shear stress limiter (BSL). The

BSL and SA simulations are run until the residuals decrease to values of 10^{-11} . However, the KW simulation exhibits a slight unsteadiness in the GTS wake that does not converge below 10^{-7} .

1. Velocity Field

Figure 12 shows the medium grid BSL solution using particle traces that are colored by the z -component velocity magnitude around the GTS model. This figure shows a relatively simple flow structure with no massive flow separation or vortex structures except for those in the trailer wake. Figures 13-16 present the flow field around the GTS model. Figure 13 shows the velocity magnitude contours at the symmetry plane ($y/w=0$) around the GTS geometry. This figure highlights the boundary layer growth on top of the trailer, as well as the velocity field around the tractor and under the GTS model. It also shows the flow accelerating between the four support posts. Figure 14 shows the velocity field on the horizontal cut-plane ($z/w=0.930$). The boundary layer growth on the side of the GTS and the tractor flow field are clearly visible. Figure 15 shows the velocity magnitude field around the GTS supports and its interaction with the wake. Figure 16 presents the velocity field on the vertical cut-plane ($x/w=4.692$). This figure shows the influence of the supports and the tunnel boundary layer at the trailer mid-length. At this yaw angle, all turbulence models produce similar velocity fields as those depicted in Figs. 12-16.

2. Aerodynamic Forces

Table 5 shows the computed aerodynamic force coefficients for the selected turbulence models and the experimental data. Among the selected models, BSL shows the closest agreement to the experimental data. The medium and coarse mesh drag coefficients are to within 0.3% and 2% of the experimental drag coefficient, respectively. The KW model under predicts the drag coefficient by about 10% and the SA model over predicts the drag coefficient by about 21%. For the lift coefficient, all models yield a similar result with the difference ranging from 33% for the KW model to about 18% for the SA model. All models predict the side force to within the experimental uncertainty range of 133%. The BSL model produces a similar result for the lift and side forces on the medium and coarse meshes. Since the differences in computed drag coefficients are primarily due to the pressure contribution, it is useful to examine the pressure field around the GTS model.

3. Surface Pressure

Figures 17-21 present a comparison of the computed pressure coefficients for all turbulence models to the experimental pressure tap data. The uncertainty in the pressure coefficients is not shown since the error bars are approximately equal to the size of the symbols used in these figures. Figure 17 compares the data of the 3 pressure taps in front of the GTS (stagnation area) to the computed solution. Figures 18 and 19 show a comparison of the pressure coefficient distribution on the top and the bottom of the GTS to that of the experimental data. Again, the agreement is reasonable except for the top of the trailer close to the base. Figure 20 shows the computed pressure coefficient on the port side of the GTS at the mid-section of the trailer compared to the experimental data. At the tractor, there is a slight difference, which improves as one move towards the base. Figure 21 displays the comparison of the pressure coefficients to the experimental data at the trailer base. It is clear that none of the turbulence models capture either the pressure field magnitude or trend. Figure 22 shows the comparison of the computed pressure coefficients from the symmetry plane toward the edge of the trailer. The computed results fail to capture the correct trend and magnitude of pressure field over the entire surface of the trailer base. Overall, the RANS models yield a realistic pressure field on the body of the GTS with the exception of the trailer base.

To investigate the mesh resolution influence on the pressure field, a coarse mesh simulation is performed using the BSL model. Figures 23-25 present a grid convergence study for the BSL turbulence model at 0° yaw. Both the coarse and medium grids produce a similar solution around the GTS except for the trailer base where a slight difference is observed.

4. Separated Flow Structure

To better understand the trailer wake flow structure, a comparison is made between the computed solutions and the time-averaged PIV data. The mid-height horizontal PIV data (Fig. 26) shows the existence of two dominant counter-rotating vortices. The results for all three turbulence models (Figures 27-29) capture these vortices at different axial and spanwise locations as summarized in Table 6. The vortex locations from the KW model appear most similar to those of the experimental data.

Figure 30 presents particle traces using the PIV data at the cross-stream plane ($x/w=8.451$). It is difficult to ascertain the dominant flow features in this PIV plane. The solutions of all the three turbulence models show the

greatest difference (Figures 31-33) in this cut-plane. The BSL model does not display any vortex-like structure in this plane. The KW model shows a single vortex away from the model centerline, while the SA model displays four distinct vortices in this plane. Figure 34 presents particle traces for the PIV data at the streamwise cut-plane ($y/w=0$). None of the turbulence models (Figs. 35-37) display the behavior shown in PIV data: namely, the presence of a single vortex in the lower half of the sheet. In addition, KW is the only model that exhibits any significant vertical asymmetry. This particular cut-plane clearly illustrates the disparity in recirculation zone size among the turbulence models.

B. Results for 10° Yaw

Run 7 point 5 with the GTS baseline configuration at 10° yaw is selected from the NASA experiment⁵ for simulation. The same boundary conditions are maintained as those used in the 0° yaw simulations. Two grids are generated for this case. The statistics for these meshes are presented in Tables 2 and 3. For this yaw angle, the computed Mach number at the pressure ring location is to within 0.5% of the experimental value. The simulations shown in Table 7 are performed at 10° yaw. The BSL and SA simulations are run until the residuals decrease to values of 10-11. Again, the KW simulation exhibits a slight unsteadiness in the GTS wake, preventing the residuals from converging below 10-7.

1) Velocity Field

Figure 38 presents the BSL solution on the medium grid using particle traces that are colored by the z -component of velocity. This figure shows a complex flow structure with multiple flow separations and vortices around the GTS model. Figure 39 shows the velocity field using the velocity magnitude contours at the trailer mid-height ($z/w=0.930$), suggesting a recirculation zone on the leeward side of the GTS. Figure 40 shows a horizontal plane at $z/w=0.1175$, corresponding to a support post mid-height. An interesting interaction is observed between the wakes of the posts with the background and trailer wake flows. Figure 41 shows a plane of velocity magnitude contours at the trailer mid-length, highlighting the complexity of the flow under yawed conditions. There appears to be a strong interaction between the flow around the GTS and the tunnel boundary layer.

2) Aerodynamic Forces

Tables 8 and 9 present the computed aerodynamic force coefficients for the selected turbulence models compared to the experimental data. The drag and lift coefficients are within the experimental uncertainty of ± 0.01 ; however, the side force coefficient shows a difference of 0.128, which is larger than the experimental uncertainty. The computed results are compared to the averaged experimental values of the $\pm 10^\circ$ yaw angles. The BSL model produces a drag coefficient that is within 3.9% of the experimental data. The drag coefficient computed from the KW model is to within 5.4% of the experimental data, while that from the SA model is to within 17.5%. The drag coefficient from the BSL model on the coarse mesh is to within 5.3% of the experimental data. All turbulence models predict lift coefficients that differ from the experiment by more than 200%. Additionally, the sign of the lift coefficient is not captured correctly. However, all turbulence models reasonably yield a side force coefficient to within 4.6-5.2% of the experimental data. The BSL coarse mesh results generates a 5.6% difference in the side force. Overall, drag coefficient is computed reasonably well, except for the SA model in which the lift coefficient is not captured at all. The side force coefficient is adequately produced by all the turbulence models.

To investigate the influence of the discretization order on the advective part of the turbulence equations, two simulations are performed using the BSL model on coarse and medium meshes. Table 9 presents the computed force coefficients for these two runs. The results of the computed lift and drag coefficients are 79% and 0.5%, further from the experimental data, respectively. The side force coefficient improves by 0.8% of the experimental value. For the GTS RANS calculations, the influence of the turbulence advection order on the drag prediction is minor, while it is significant for the lift coefficient.

3) Surface Pressure

To further investigate the pressure contribution to the aerodynamic forces, the pressure field around the GTS at 10° yaw is compared to the experimental data. Figures 42-48 present comparisons of the computed and experimental pressure coefficients. There is good agreement between the computed and experimental pressure coefficients on the front of GTS in Figure 42. Figure 43 compares the pressure coefficient distribution on top of the GTS to the experimental data. The agreement between the two is reasonable, except for the area close to the base of the trailer, where the BSL and KW models depart significantly from the experiment. The SA model

displays the correct trend, but does not fully capture the data. A similar behavior is observed for the 0° yaw case, but to a somewhat lesser extent. Figure 44 shows a comparison of the pressure coefficients on the bottom of the GTS. The pressure recovery under the tractor does not match the experimental data, but the computed result displays the correct trend. In contrast, the computed result beneath the trailer does not display the correct trend compared to the experimental data. The agreement between the simulations and the experimental data improves towards the trailer base.

Figure 45 presents the pressure coefficients on the windward side of the GTS compared to the experimental data. Near the stagnation area, there is a slight difference, which decreases toward the trailer base. This may be due to the experimental uncertainty in the yaw angle. Figure 46 presents a comparison of the pressure coefficients to the experiment on the leeward side of the GTS. The agreement is reasonable on the trailer; however, there is some disagreement in the area of rapidly varying pressure. Figure 47 shows the pressure coefficient distribution on the trailer base compared to the experimental data. There is significant disagreement between the computed result in both trend and magnitude. Figure 48 shows the pressure distribution on the base of the trailer from the trailer center towards the outer edge. The disagreement between the computed and experimental results is apparent over half of the trailer base. The 2nd-order treatment of the turbulence equations does not alter the previously reported pressure coefficients, except for those on the base as shown in Fig. 49. This minor variation may be responsible for the change in the drag prediction (Table 9). With the exception of the trailer top and base, all turbulence models reasonably capture the pressure field over the GTS. To investigate the mesh resolution influence on the pressure field, a coarse mesh simulation is performed using the BSL turbulence model (Figs. 50-52). Both the coarse and the medium meshes produce similar solutions around the GTS except at the trailer base, suggesting adequate resolution of the pressure field.

4) Separated Flow Structure

To investigate the trailer wake flow structure, a comparison is made between the computed solutions and the time-averaged PIV data. Figure 53 presents the PIV data using particle traces for the horizontal laser sheet located at the trailer mid-height ($z/w=0.930$). This figure suggests the presence of three vortices in the wake. The BSL and SA models (Figs. 54 and 56) capture two vortices, but show no possibility of a third. The KW model shown in Fig. 55 does not display either of the vortices on the leeward side of the wake; however, the unusual trace pattern suggests that some of the vortex effects are captured. Table 10 shows the positions of the vortices relative to the center of the trailer base. The vortex locations from the BSL model appear most similar to those of the experimental data. The PIV particle traces in a plane located parallel to and $1.137w$ behind the trailer base (Fig. 57) highlight a dominant vortex in the wake. The corresponding particle traces from the computed results are shown in Figs. 58 to 60. The BSL model exhibits a stable focus in a position similar to that seen in the experimental data. The particle traces from both the KW and SA model show additional vortex structures near the bottom of the wake. In contrast to the KW and BSL models, the SA model predicts the flow structure on the leeward side of the trailer base. Given the above comparisons, the computed wake flow structure is significantly different from the PIV data.

At this yaw angle, multiple vortex structures are present in the vicinity of the GTS body as highlighted in Fig. 41. The position of the vortex that rolls-up on top of the trailer is compared qualitatively to the surface shear stress vector data (Fig. 61) obtained from the oil film interferometry.⁵ Figures 62-64 present the particle traces confined to the top of the GTS for all turbulence model calculations. Two lines are drawn over these images representing the separation and reattachment lines obtained from the experimental data. Note that there is an uncertainty associated with the position of these lines because the surface shear stress vector data is relatively coarse. All turbulence models clearly demonstrate the presence of a main vortex and suggest the possibility of a secondary vortex. The SA model yields separation and reattachment lines closest to the experimental data. The reattachment lines from the BSL and KW models are further from that of the main separation vortex. None of the models correctly capture the position of the second vortex.

Hot-film anemometry measurements detail the existence of a separation bubble on the leeward side of the GTS.⁵ Particle traces on the leeward side of the GTS (Figs. 65-67) show multiple reattachment and separation zones. The BSL and KW models show analogous vortex footprints on the model surface; however, the SA model predicts a significantly different flow pattern. Interestingly enough, the side forces for the three models (Table 8) do not display much sensitivity to these different flow patterns.

X. Conclusions

Validation simulations of simplified tractor/trailer geometry at 0° and 10° yaw are performed to highlight the predictive capability of selected RANS turbulence models. The results of this effort contribute to the heavy vehicle aerodynamics initiative sponsored by the Department of Energy Office of Heavy Vehicle Technologies. At 0° yaw, the Menter $k-\omega$ (BSL) model predicts the aerodynamic drag to within the uncertainty of the experimental data. The surface pressures at 0° yaw reasonably match those of the experiments, except for those located on the trailer base. The wake flow structure from the simulations varies among the models with KW producing the most realistic results. For the 10° yaw cases, the BSL model once again yields a drag coefficient closest to that of the experimental data, although the top and bottom surface pressures differ slightly. In contrast, the base surface pressures from the simulations and experiment disagree in both magnitude and trend. The BSL trailer wake flow structure is most representative of the PIV data. On the other hand, the SA model displays the most reasonable vortex footprint on the top surface of the trailer. The grid convergence study demonstrates that adequate resolution is given the resolve the simulated flow structures.

Acknowledgments

The authors wish to thank Bruce Storms, Jim Ross, Steve Walker, J.T. Heineck, and Dale Satran of NASA Ames for providing assistance in comparing the experimental data with the simulations results. The authors sincerely thank Helen Magann of LLNL for her administrative support in the preparation of this manuscript. This work was funded by the Department of Energy Office of Heavy Vehicles Technologies under the direction of Sid Diamond and Jules Routbort.

References

- ¹Highway Statistics, US. Government Printing Office, SSOP, Washington DC 20402-9328, 1992
- ²Cooper, K.R., "Truck Aerodynamics Reborn—Lessons from the Past," SAE Paper No. 2003-01-3376, 2003.
- ³Gutierrez, W. T., Hassan, B., Croll, R. H., Rutledge, W. H., "Aerodynamics Overview of the Ground Transportation Systems (GTS) Project for Heavy Vehicle Drag Reduction," SAE Paper No. 960906, Feb. 1996.
- ⁴Steen, G., "Subsonic Wind Tunnel Test of the Sandia National Laboratories Ground Transportation Vehicle," TEES Report No. TR-9514, July 1995.
- ⁵Storms, B., et. al., "An Experimental Study of the Ground Transportation System (GTS) Model in the NASA Ames 7-by 10-Ft Wind Tunnel," NASA/TM-2001-209621, Feb. 2001.
- ⁶Hassan, B., Gutierrez, W. T., Wolfe, W., Walker, M., "Numerical Prediction of Aerodynamic Drag for Heavy Ground Transportation Vehicle," AIAA Paper AIAA-95-1913, June 1995.
- ⁷Maddox, S., Squires, K.D., Forsythe, J.R., Detached-Eddy Simulation of the Ground Transportation System, United Engineering Foundation, The Aerodynamics of Heavy Vehicles: Trucks, Buses and Trains, Pacific Grove, California, November, 2002, to be published.
- ⁸Salari, K. and McWherter-Payne, M., "Computational Flow Modeling of a Simplified Integrated Tractor-Trailer Geometry," Sandia Report SAND2003-3383, 2003.
- ⁹Spalart, P.R. Allmaras, S.R., A One-Equation Turbulence Model for Aerodynamic Flows, AIAA Paper 92-439, Reno, NV, 1992.
- ¹⁰Wilcox, D.C., *Turbulence Modeling for CFD*, 2nd Edition, DCW Industries, 1998.
- ¹¹Menter, F.R., Two-Equation Eddy-Viscosity Turbulence Models for Engineering Applications, AIAA J., 32 (8), 1994, 1598-1605.

Table 1. Laser sheet orientations (Ref. 3).

Orientation	Location	Yaw	Re / 10⁶
Horizontal	y/w = 0.35, 0.70, 1.05	0°, 10°	2.0, 0.74, 0.3
Cross-stream	x/w = 8.00, 8.35, 8.78	0°, 10°	2.0, 0.74
Streamwise	z/w = 0.0	0°	2.0, 0.74

Table 2. Coarse mesh statistics for 0° and 10° yaw.

Yaw angle	No. of elements	Min spacing in x	Min spacing in y	Min spacing in z
0° yaw	11.8 M	0.20 mm	0.20 mm	0.20 mm
10° yaw	14.0 M	0.20 mm	0.20 mm	0.20 mm

Table 3. Medium mesh statistics for 0° and 10° yaw.

Yaw angle	No. of elements	Min spacing in x	Min spacing in y	Min spacing in z
0° yaw	14.0 M	0.19 mm	0.19 mm	0.19 mm
10° yaw	19.0 M	0.19 mm	0.19 mm	0.19 mm

Table 4. Run matrix for the 0° yaw.

Mesh	Turbulence Model		
	BSL	KW	SA
Medium	x	x	x
Coarse	x		

Table 5. Computed aerodynamic forces for the GTS model at 0° yaw.

Medium grid, BSL		CD	Error	CL	Error	CS	Error
	Pressure	0.1897		-0.1226		-1.4E-05	
	Viscous	0.0741		0.0012		-1.5E-07	
	Total	0.2638	0.3%	-0.1214	24.1%	-1.4E-05	-100%
Medium grid, KW		CD		CL		CS	
	Pressure	0.1603		-0.1083		-4.3E-04	
	Viscous	0.0775		0.0013		-8.1E-07	
	Total	0.2377	-9.6%	-0.1070	33.1%	-4.3E-04	-106%
Medium grid, SA		CD		CL		CS	
	Pressure	0.2435		-0.1329		5.3E-05	
	Viscous	0.0737		0.0012		-2.3E-06	
	Total	0.3173	20.6%	-0.1317	17.7%	5.1E-06	-99%
Coarse grid, BSL		CD		CL		CS	
	Pressure	0.1943		-0.1232		-1.1E-06	
	Viscous	0.0741		0.0012		-1.9E-06	
	Total	0.2684	2.0%	-0.1220	23.7%	-3.0E-06	-100%
NASA experiment ±0.01 error		CD		CL		CS	
	Point 2	0.263	±3.8%	-0.168	±6.2%	0.008	±133%
	Point 9	0.263		-0.152		0.007	
	Average Magnitude	0.263		-0.16		0.0075	

Table 6. Vortex location from trailer base center, 0° yaw.

	Δx	Δy
SA	0.473	0.348
KW	0.996	0.309
SST	0.714	0.349
PIV	0.887	0.311

Table 7. Run matrix for the 10° yaw.

Mesh	Turbulence Model			
	1 st -order BSL	2 nd -order BSL	KW	SA
Medium	X	X	X	X
Coarse	X	X		

Table 8. Aerodynamic forces for the GTS model at 10° yaw.

Medium grid, BSL		CD	Error	CL	Error	CS	Error
	Pressure	0.4804		-0.0347		1.1458	
	Viscous	0.0821		0.0027		-0.0082	
	Total	0.5626	3.9%	-0.0320	-223%	1.1376	-5.2%
Medium grid, KW		CD		CL		CS	
	Pressure	0.4866		-0.0263		1.1516	
	Viscous	0.0842		0.0027		-0.0084	
	Total	0.5708	5.4%	-0.0236	-190%	1.1431	-4.7%
Medium grid, SA		CD		CL		CS	
	Pressure	0.5641		-0.1192		1.1529	
	Viscous	0.0721		0.0030		-0.0078	
	Total	0.6361	17.5%	-0.1162	-547%	1.1451	-4.6%
Coarse grid, BSL		CD		CL		CS	
	Pressure	0.4866		-0.0281		1.1414	
	Viscous	0.0835		0.0029		-0.0084	
	Total	0.5701	5.3%	-0.0252	-197%	1.1329	-5.6%
NASA experiment ±0.01 error		CD		CL		CS	
	+10° yaw	0.540	±1.8%	0.022	±38.4%	1.264	±0.8%
	-10° yaw	0.543		0.030		-1.136	
	Average Magnitude	0.542		0.026		1.200	

Table 9. Aerodynamic force coefficients for the GTS model at 10° yaw, 2nd-order BSL.

Medium grid, BSL, 2 nd -order		CD	Error	CL	Error	CS	Error
	Pressure	0.4858		-0.0553		1.1547	
	Viscous	0.0835		0.0027		-0.0080	
	Total	0.5701	4.4%	-0.0526	-302%	1.1466	-4.4%
Coarse grid, BSL, 2 nd -order		CD		CL		CS	
	Pressure	0.4937		-0.0495		1.1449	
	Viscous	0.0795		0.0029		-0.0083	
	Total	0.5745	6.1%	-0.0466	-279%	1.1366	-5.3%
NASA experiment ±0.01 error		CD		CL		CS	
	+10° yaw	0.540	±1.8%	0.022	±38.4%	1.264	±0.8%
	-10° yaw	0.543		0.030		-1.136	
	Average Magnitude	0.542		0.026		1.200	

Table 10. Vortex location from trailer base center, 10° yaw.

	Leeward Vortex		Windward Vortex	
	Δx	Δy	Δx	Δy
SA	0.688	-0.307	0.621	0.335
KW	n/a	n/a	0.584	0.267
BSL	0.480	-0.330	0.477	0.342
PIV	0.530	-0.253	0.492	0.423

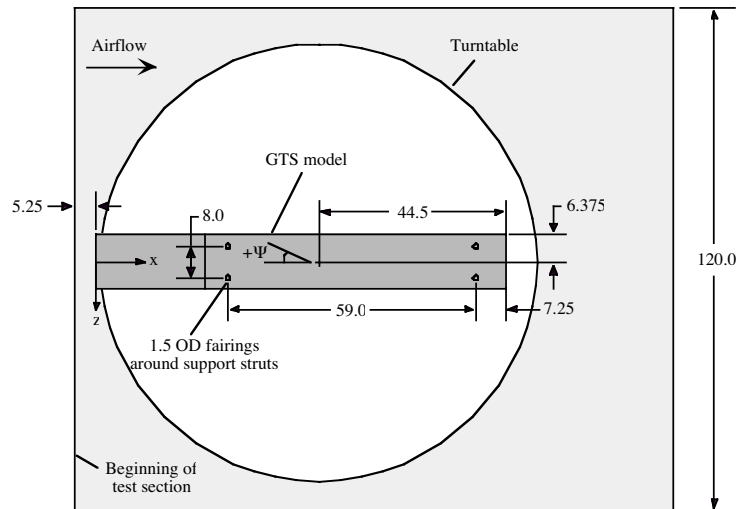


Fig. 1. GTS model installation top view (Ref. 5).

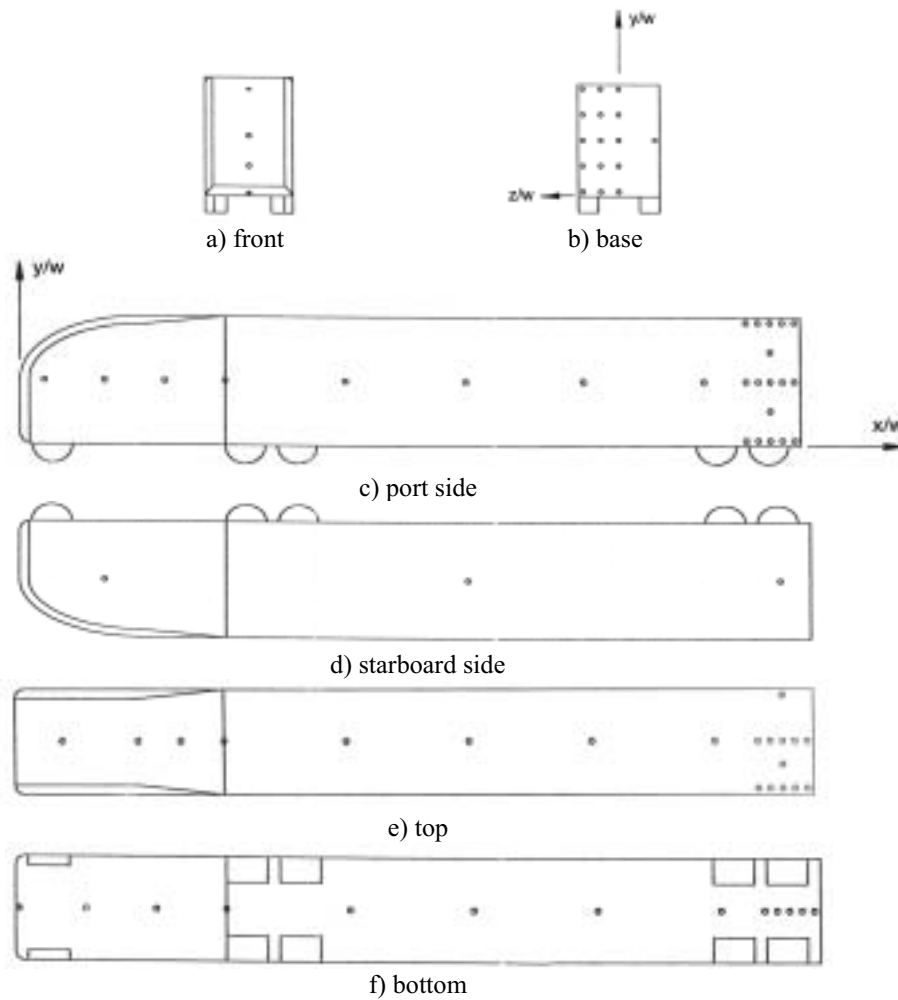


Fig. 2. Pressure tap locations on the GTS model.

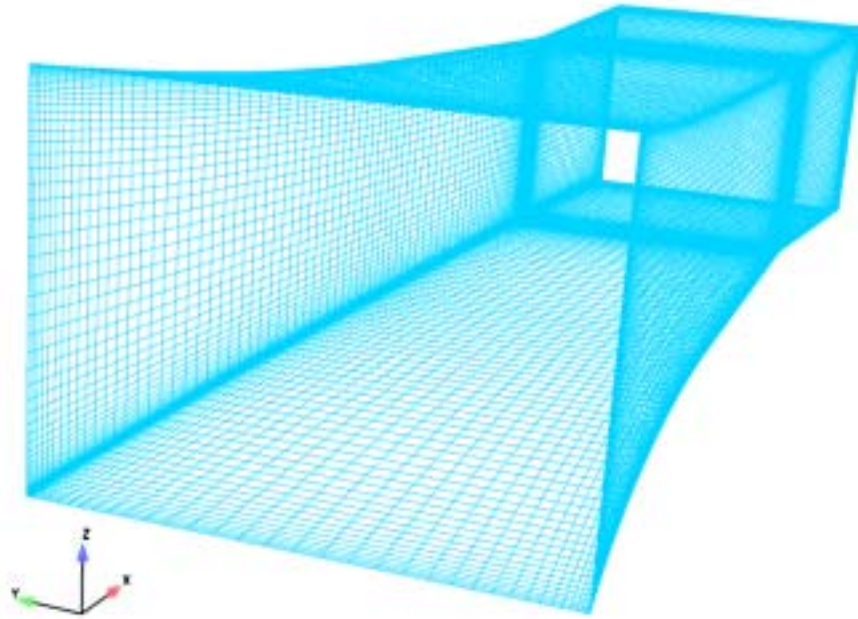


Fig. 5. Empty tunnel coarse mesh, 466,240 elements.

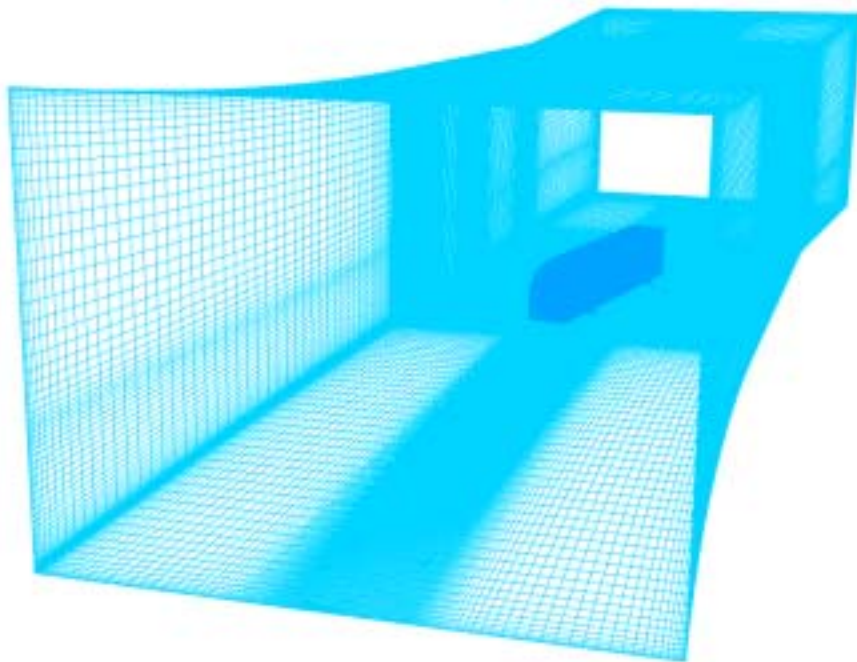


Fig. 6. GTS in NASA 7'x10' tunnel, coarse mesh, 10° yaw.

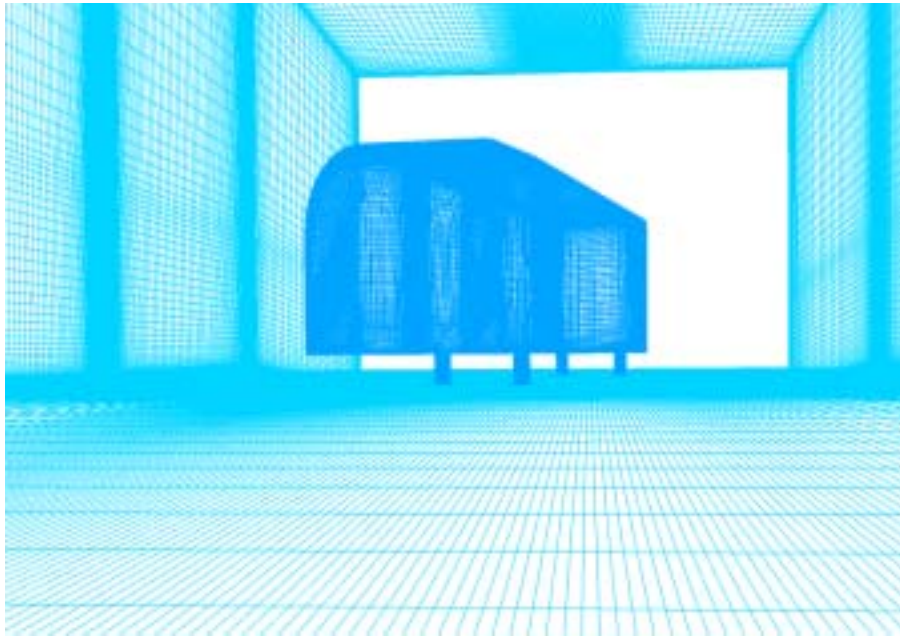


Fig. 7. GTS in tunnel mesh, coarse grid, 10° yaw.

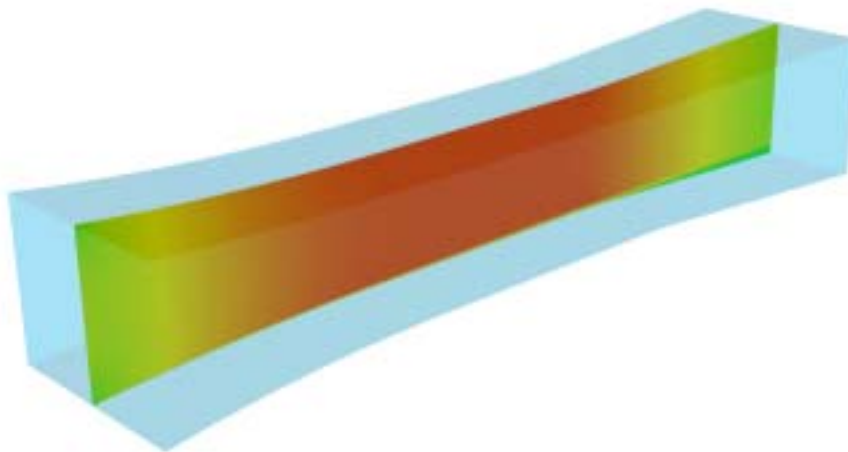


Fig. 8. Empty tunnel simulation, Mach contours, symmetry plane.

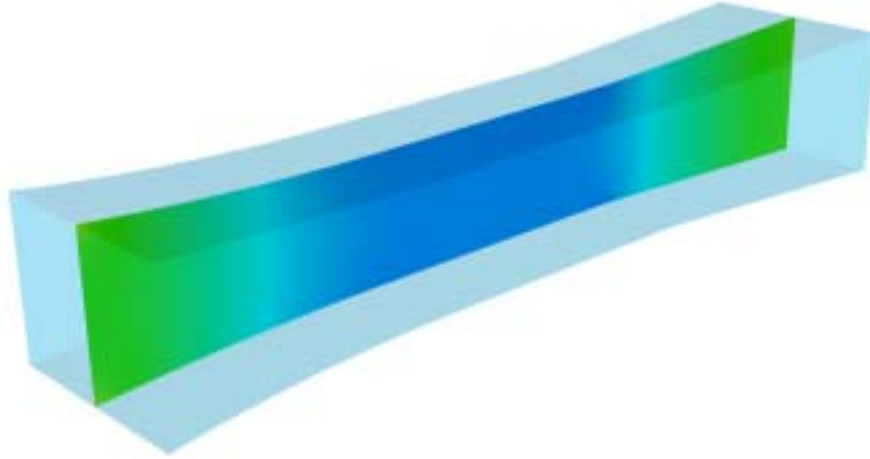


Fig. 9. Empty tunnel simulation, pressure contours, symmetry plane.

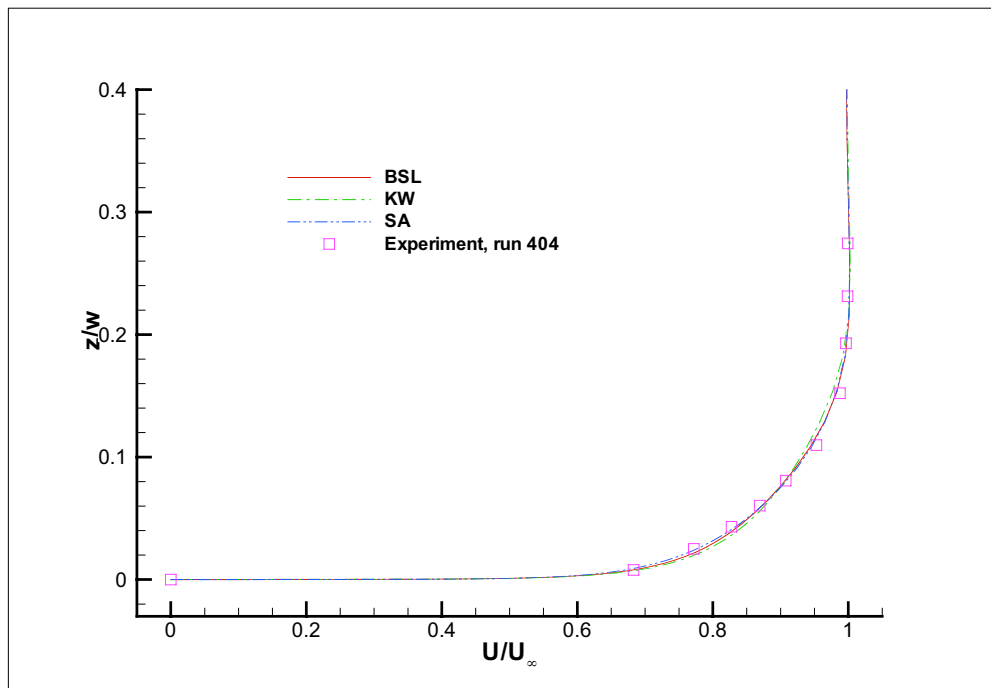


Fig. 10. Empty tunnel simulations, comparison of the computed boundary layer profiles to the NAS Ames experimental data.

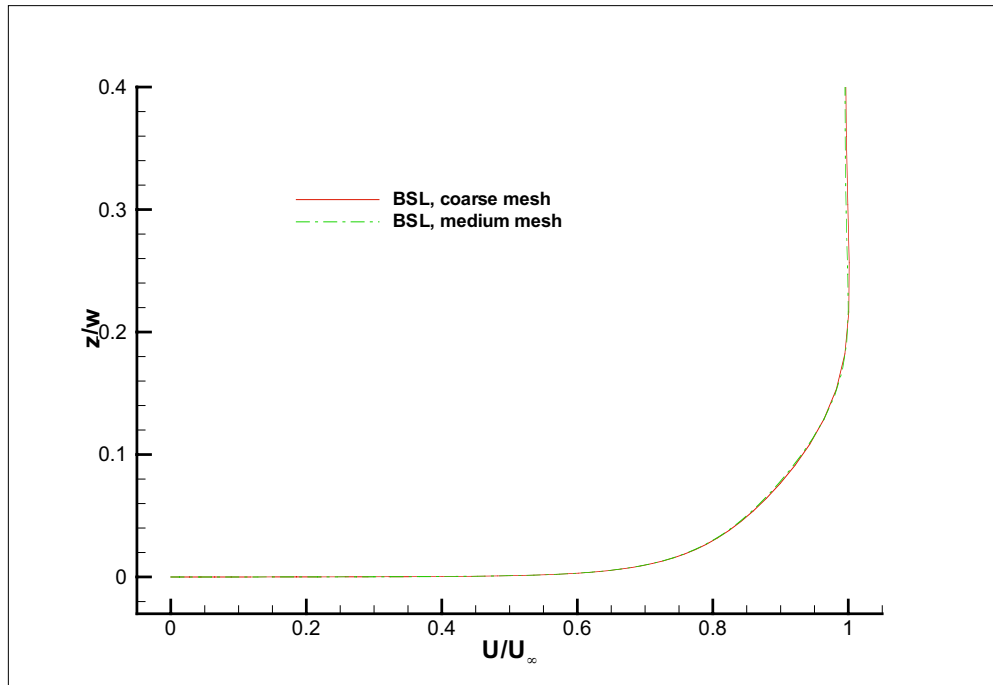


Fig. 11. Empty tunnel simulations, grid convergence study.

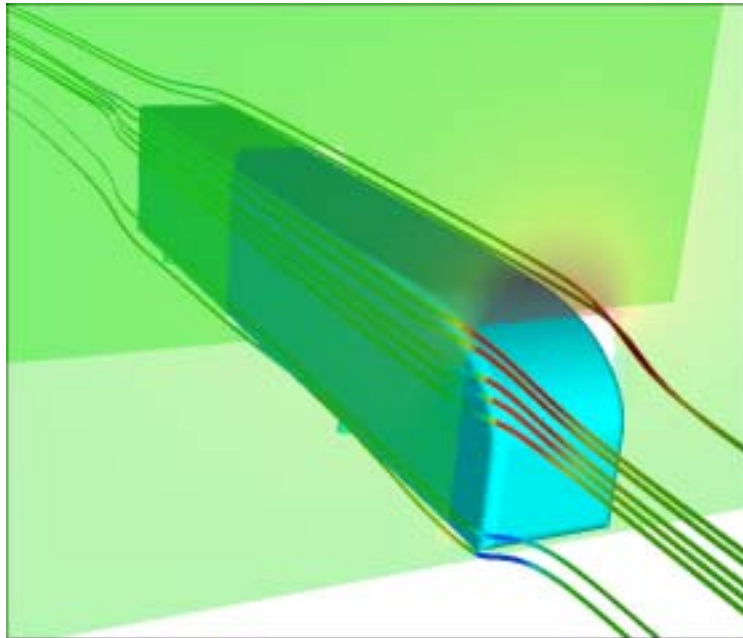


Fig. 12. GTS model particle traces colored by velocity magnitude, 0° yaw.

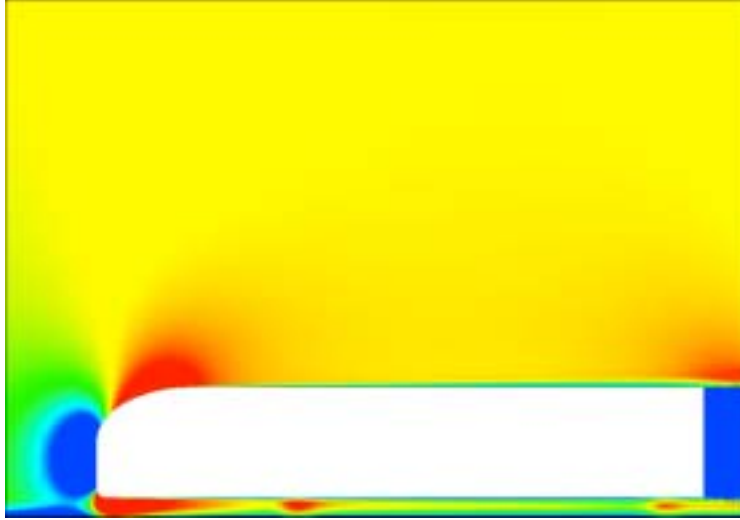


Fig. 13. Velocity magnitude contour, symmetry plane ($y/w=0$), 0° yaw.

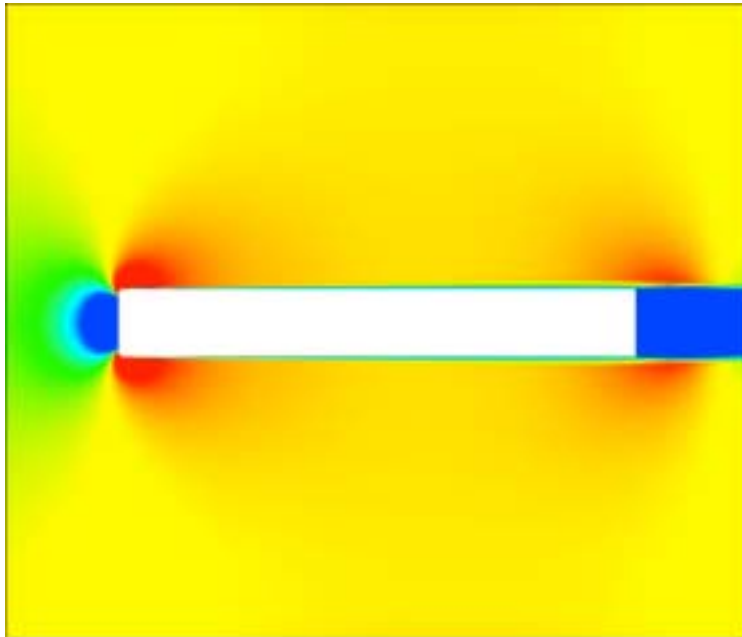


Fig. 14. Velocity magnitude contour, horizontal plane ($z/w=0.930$), 0° yaw.

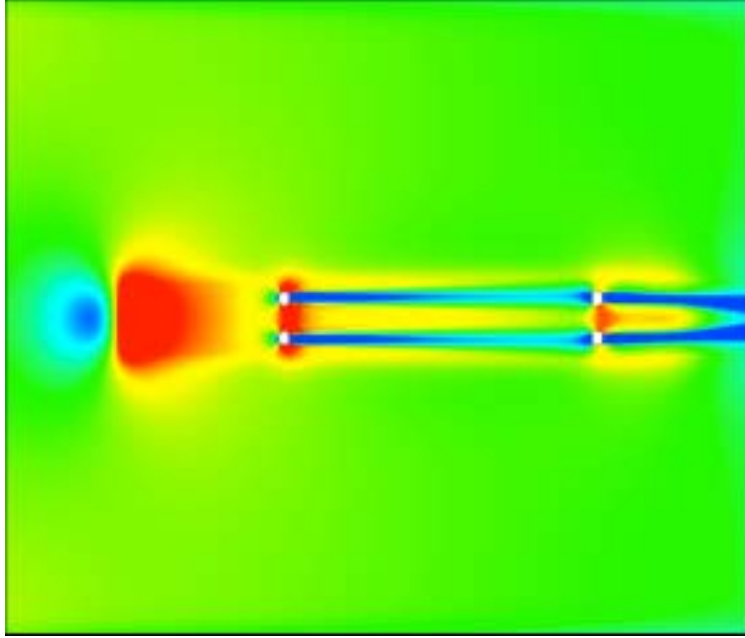


Fig. 15. Velocity magnitude contour, horizontal plane ($z/w=0.1175$), 0° yaw.

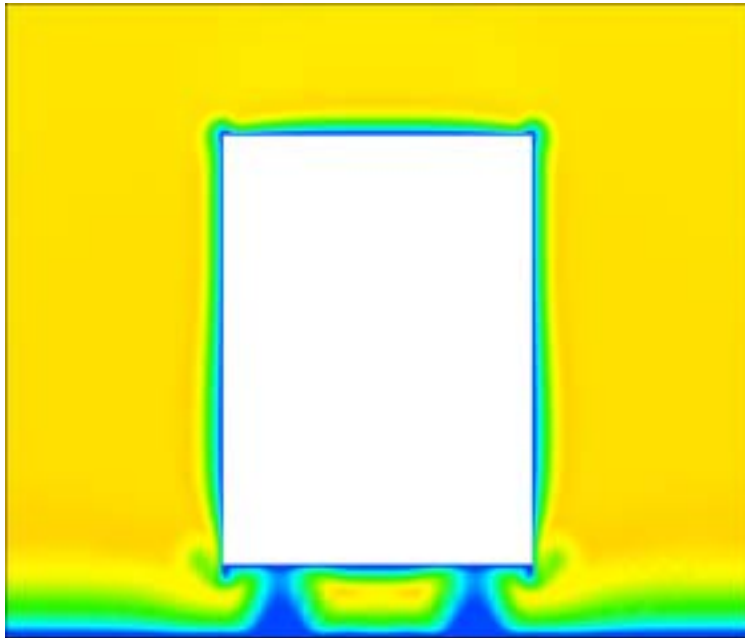


Fig. 16. Velocity magnitude contour, vertical plane ($x/w=4.692$), 0° yaw.

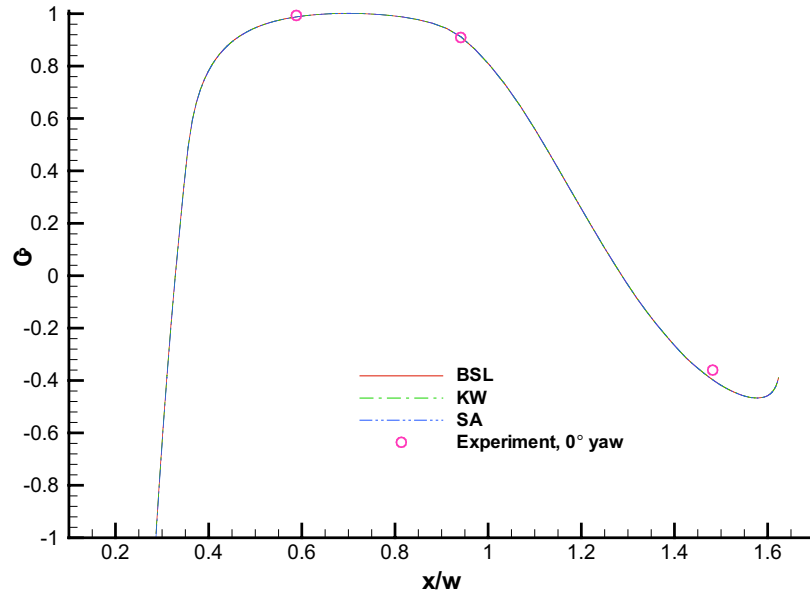


Fig. 17. Comparison of the computed C_p to the NASA experimental data, front of GTS, 0° yaw.

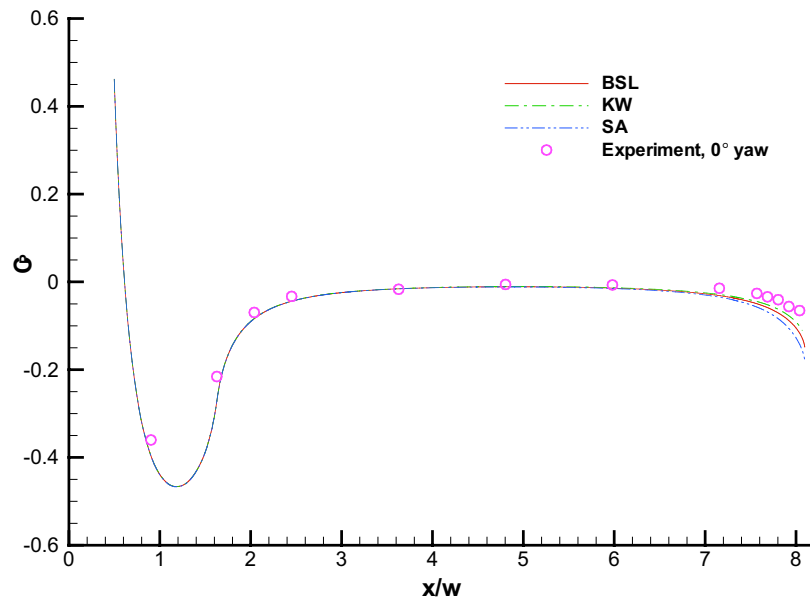


Fig. 18. Comparison of the computed C_p to the NASA experimental data, top of GTS, 0° yaw.

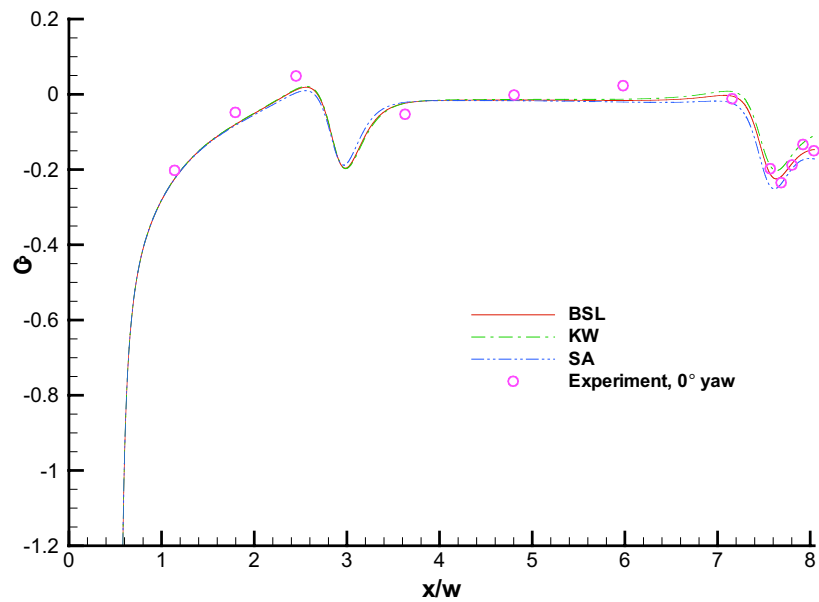


Fig. 19. Comparison of the computed C_p to the NASA experimental data, under the GTS, 0° yaw.

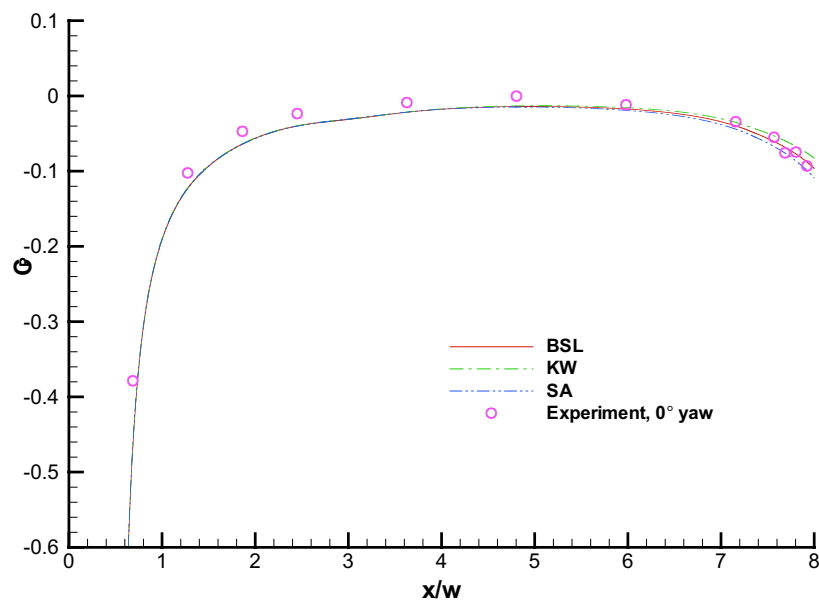


Fig. 20. Comparison of the computed C_p to the NASA experimental data, side of GTS, 0° yaw.

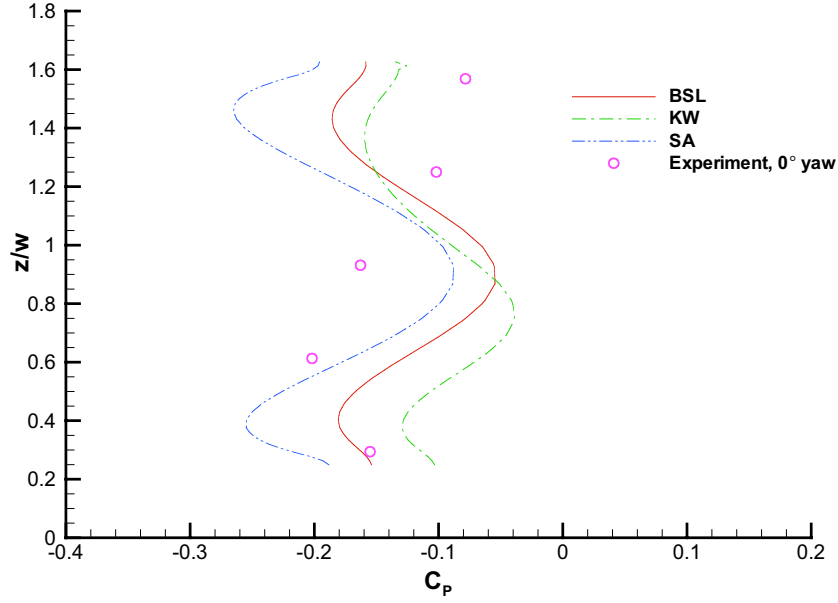


Fig. 21. Comparison of the computed C_p to the NASA experimental data, base of the GTS, 0° yaw.

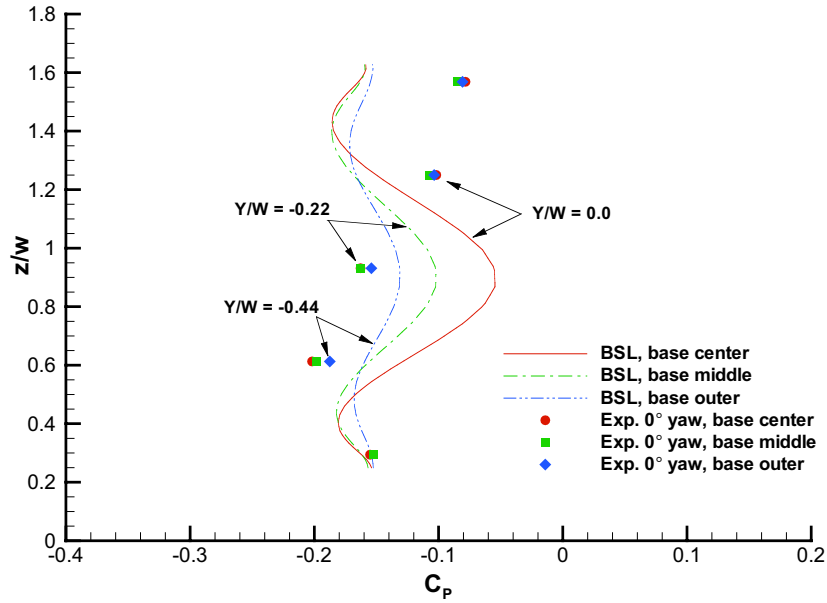


Fig. 22. Comparison of the computed C_p to the NASA experimental data, base of GTS with all pressure taps, 0° yaw.

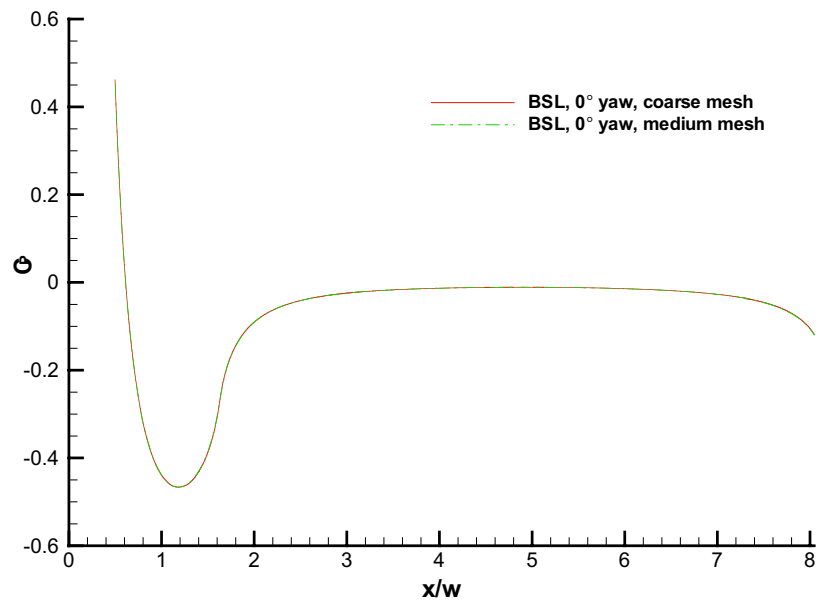


Fig. 23. Grid resolution study with BSL turbulence model, top of the GTS, 0° yaw.

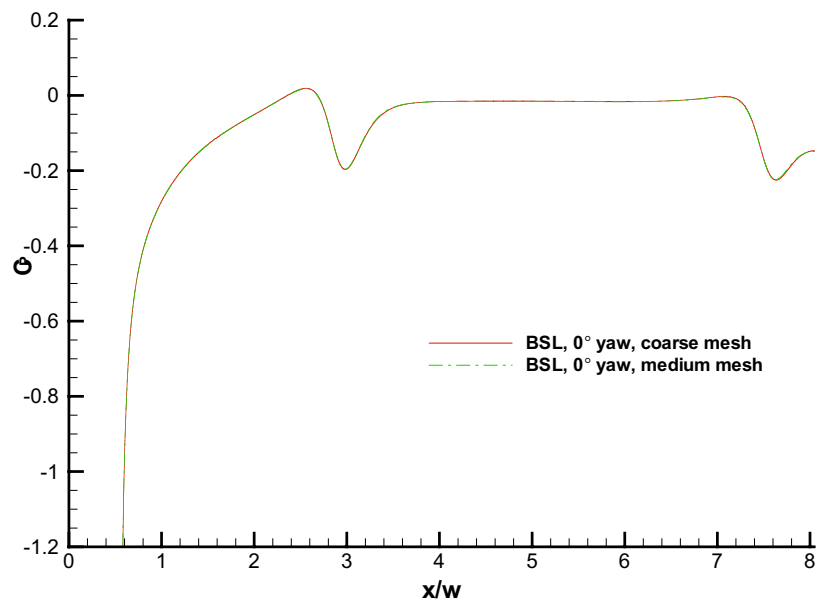


Fig. 24. Grid resolution study with BSL turbulence model, under the GTS, 0° yaw.

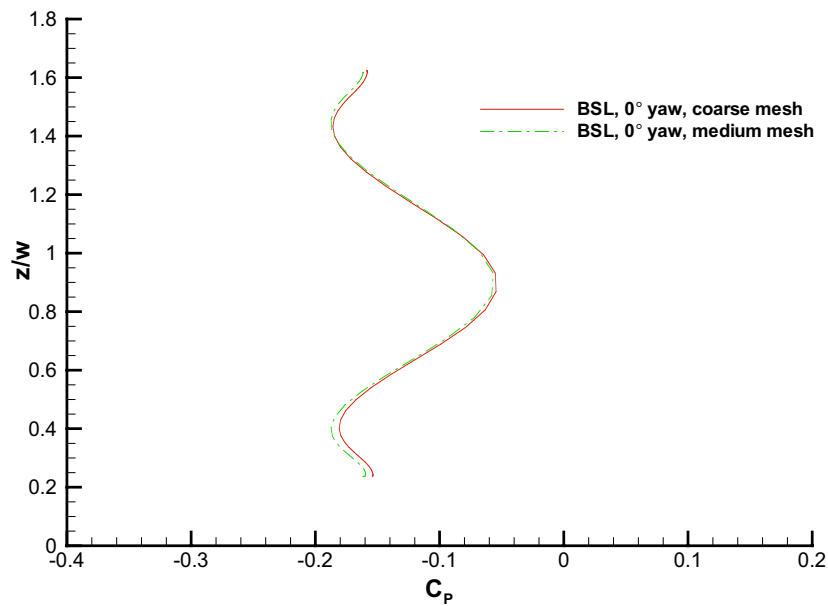


Fig. 25. Grid resolution study with BSL turbulence model, base of the GTS, 0° yaw.

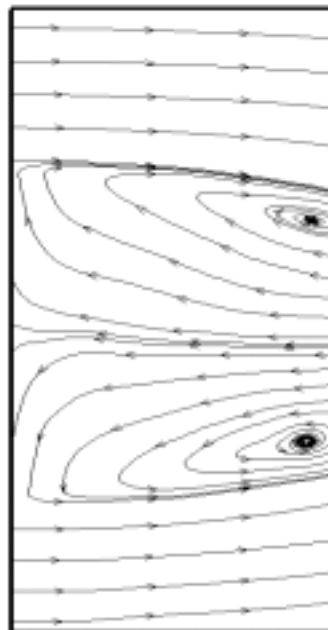


Fig. 26. Time-averaged PIV data, particle traces, horizontal laser sheet located at trailer mid-height, 0° yaw.

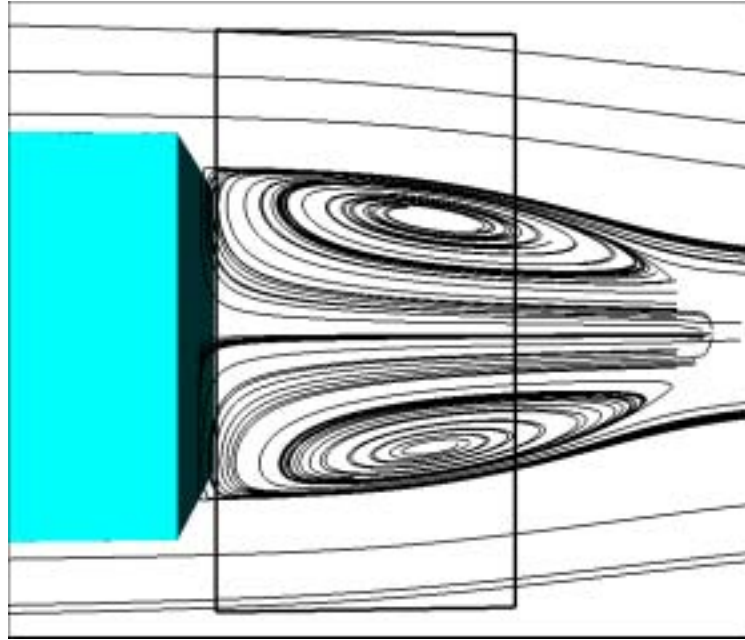


Fig. 27. Particle traces, horizontal cut-plane at trailer mid-height, BSL solution, 0° yaw.

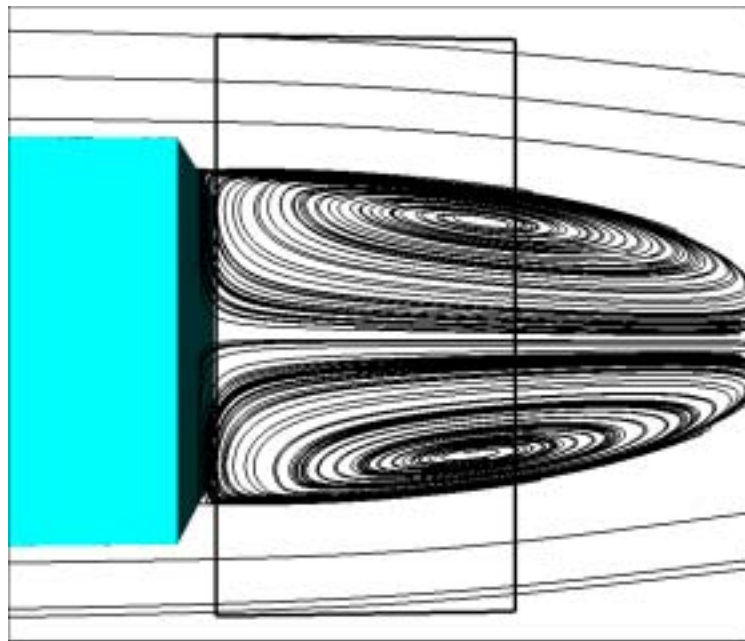


Fig. 28. Particle traces, horizontal cut-plane at trailer mid-height, KW solution, 0° yaw.

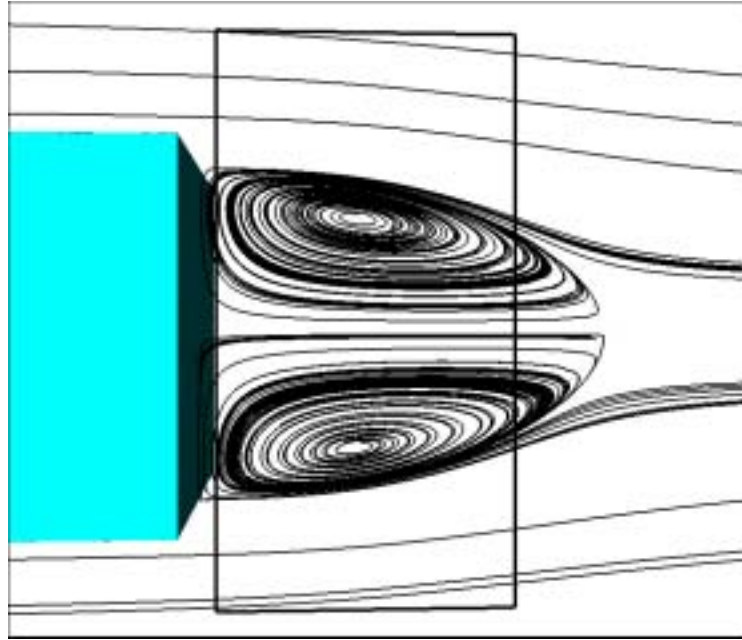


Fig. 29. Particle traces, horizontal cut-plane at trailer mid-height, SA solution, 0° yaw.

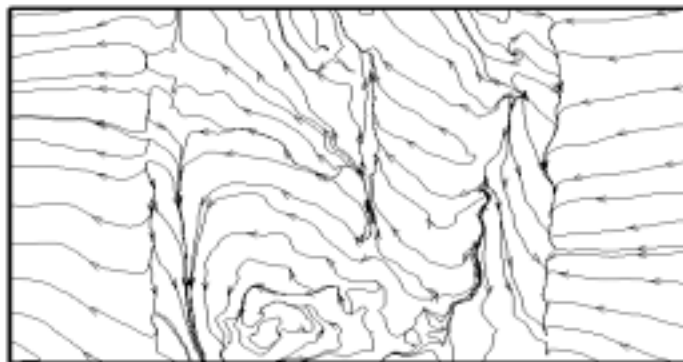


Fig. 30. Particle traces time-averaged PIV data, vertical laser sheet parallel to the base of the trailer located at $x/w=8.451$, 0° yaw.

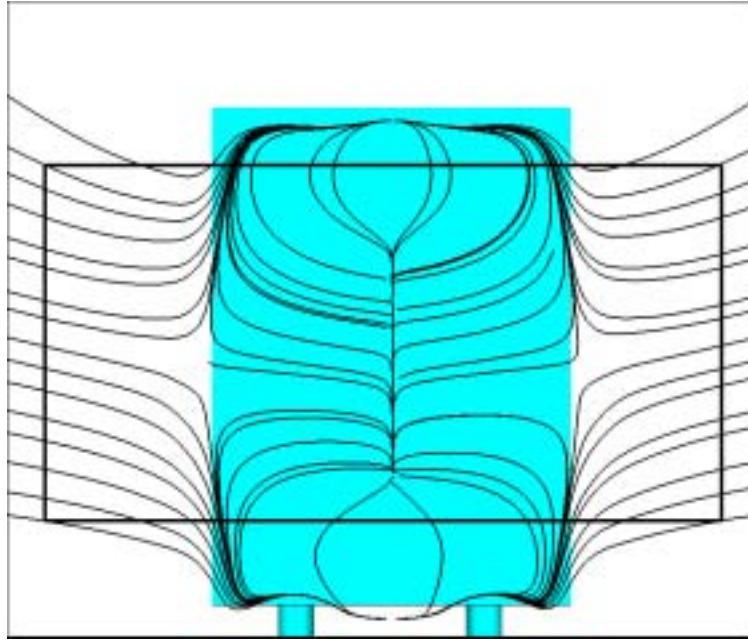


Fig. 31. Particle traces, vertical cut-plane parallel to the base of the trailer, BSL solution, 0° yaw.

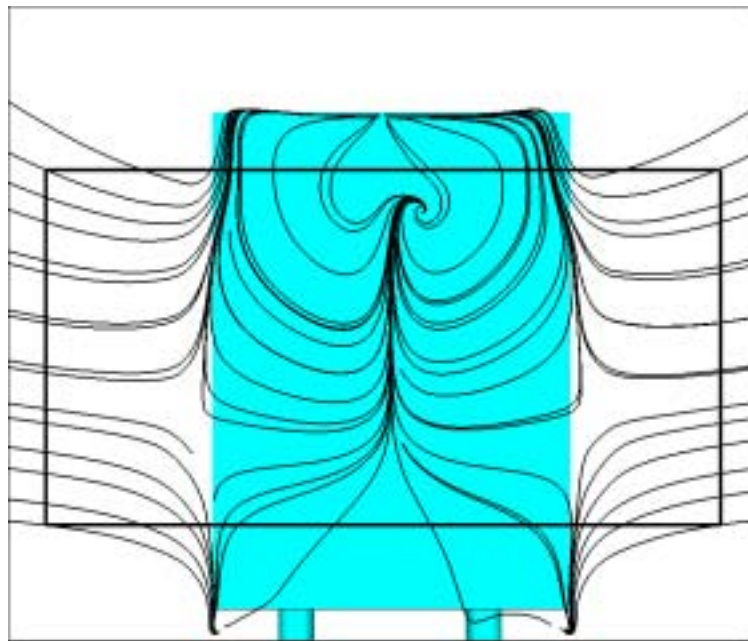


Fig. 32. Particle traces, vertical cut-plane parallel to the base of the trailer, KW solution, 0° yaw.

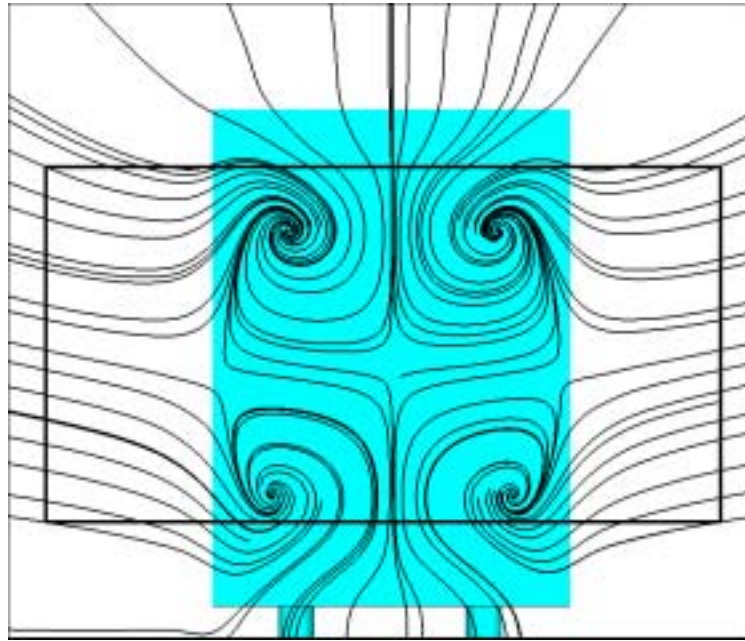


Fig. 33. Particle traces, vertical cut-plane parallel to the base of the trailer, SA solution, 0° yaw.

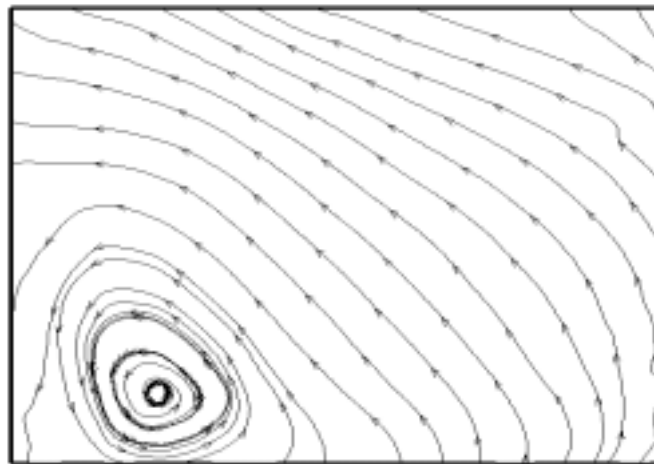


Fig. 34. Particle traces time-averaged PIV data, streamwise laser sheet located at $(y/w=0)$, 0° yaw.

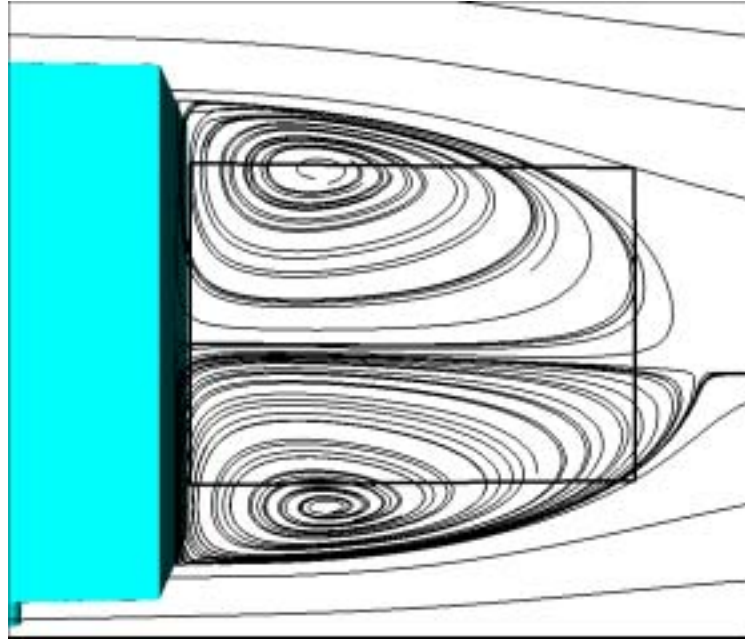


Fig. 35. Particle traces, streamwise cut-plane ($y/w=0$), BSL solution, 0° yaw.

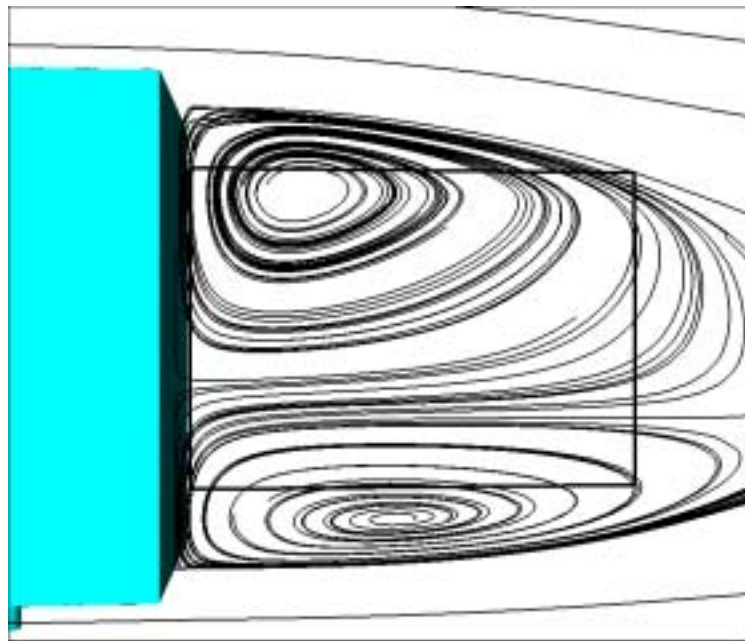


Fig. 36. Particle traces, streamwise cut-plane ($y/w=0$), KW solution, 0° yaw.

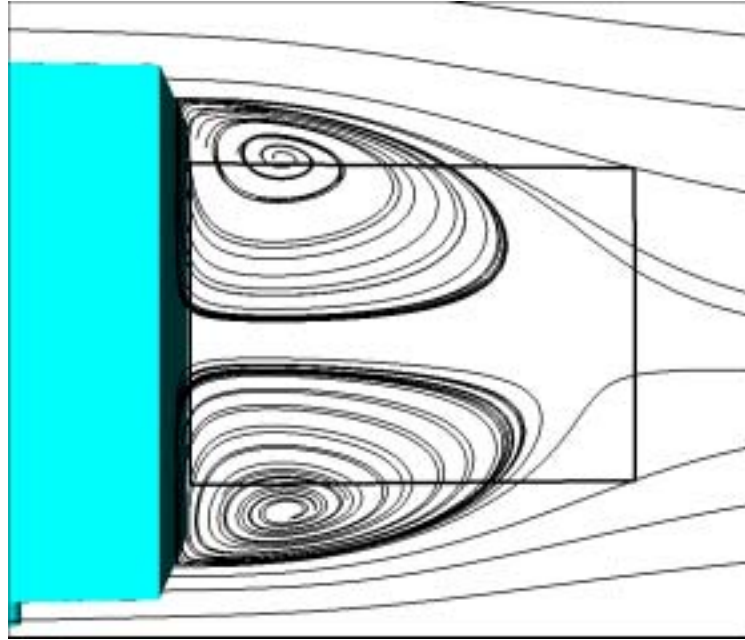


Fig. 37. Particle traces, streamwise plane ($y/w=0$), SA solution, 0° yaw.

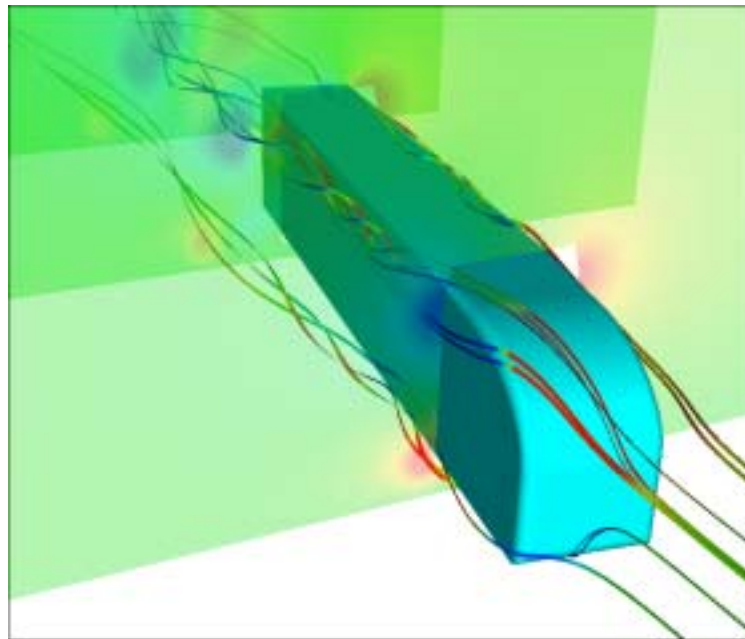


Fig. 38. Particle traces, streamwise plane ($y/w=0$), SA solution, 0° yaw.

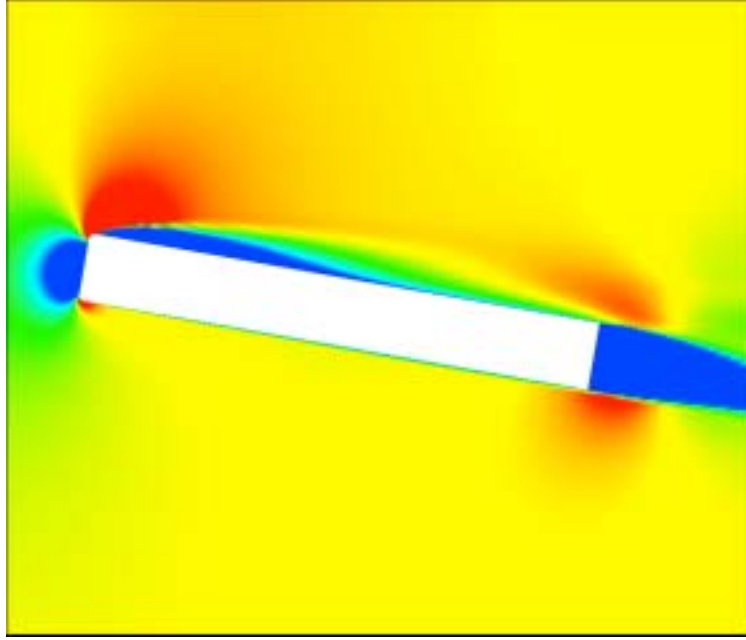


Fig. 39. Velocity magnitude contour, horizontal plane ($z/w=0.93$), 10° yaw.

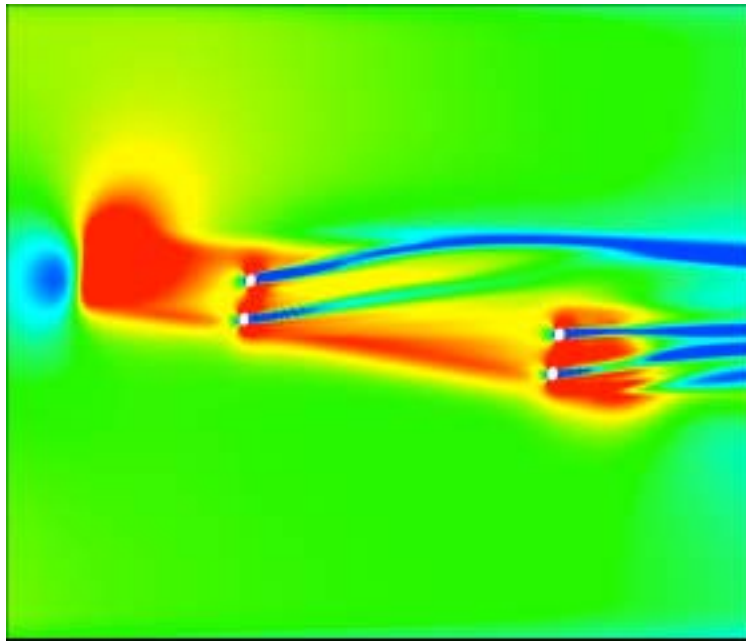


Fig. 40. Velocity magnitude contour, horizontal plane ($z/w=0.12$), 10° yaw.

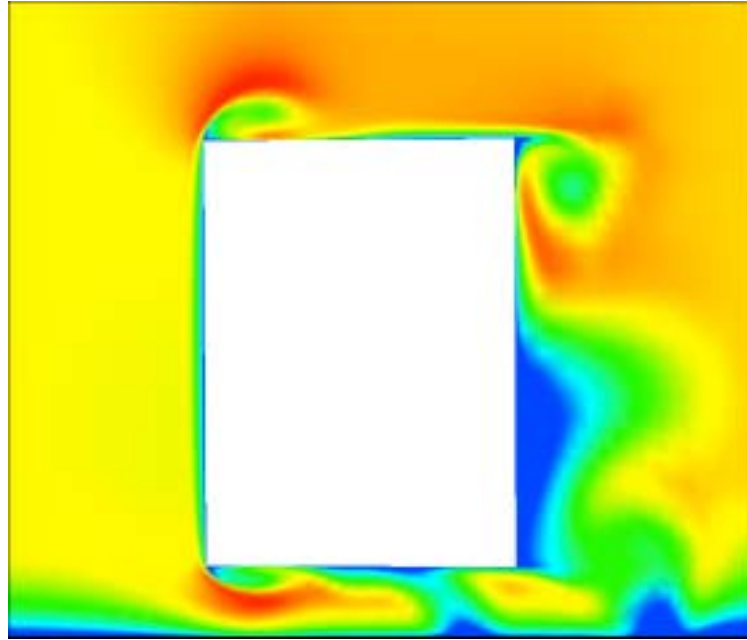


Fig 41. Velocity magnitude contour, vertical plane (trailer mid-length), 10° yaw

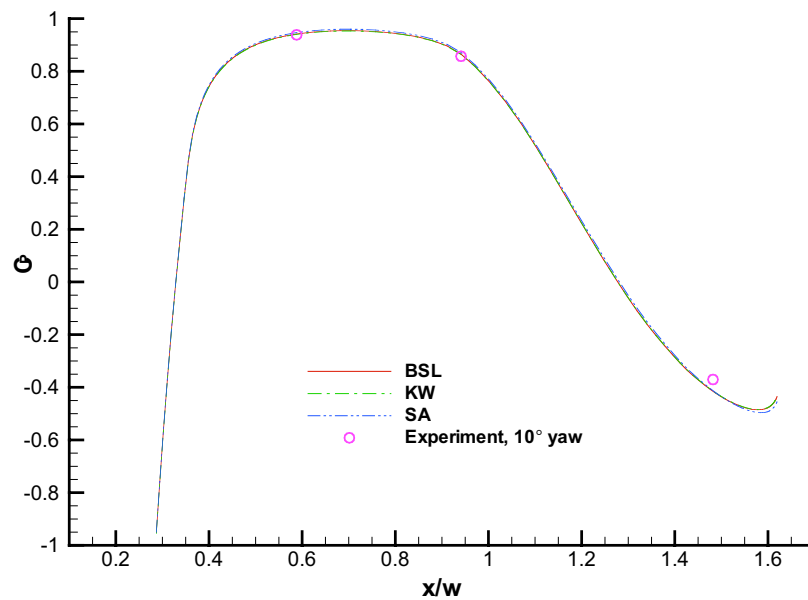


Fig. 42. Comparison of the computed C_p to the NASA experimental data, front of GTS, 10° yaw.

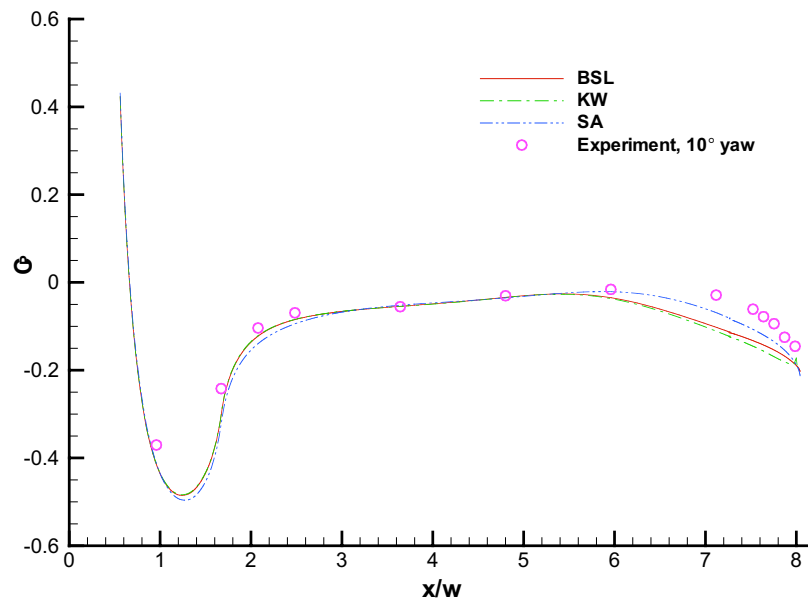


Fig. 43. Comparison of the computed C_p to the NASA experimental data, top of GTS, 10° yaw.

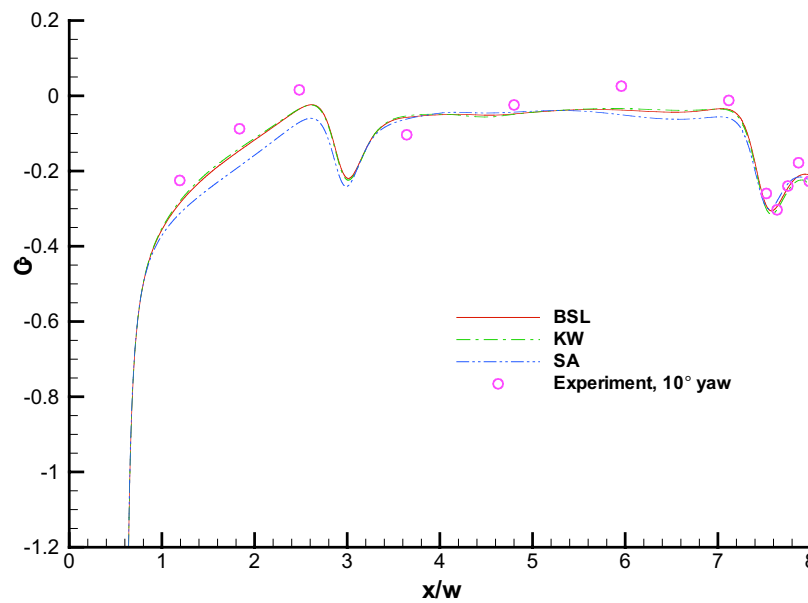


Fig. 44. Comparison of the computed C_p to the NASA experimental data, bottom of GTS, 10° yaw.

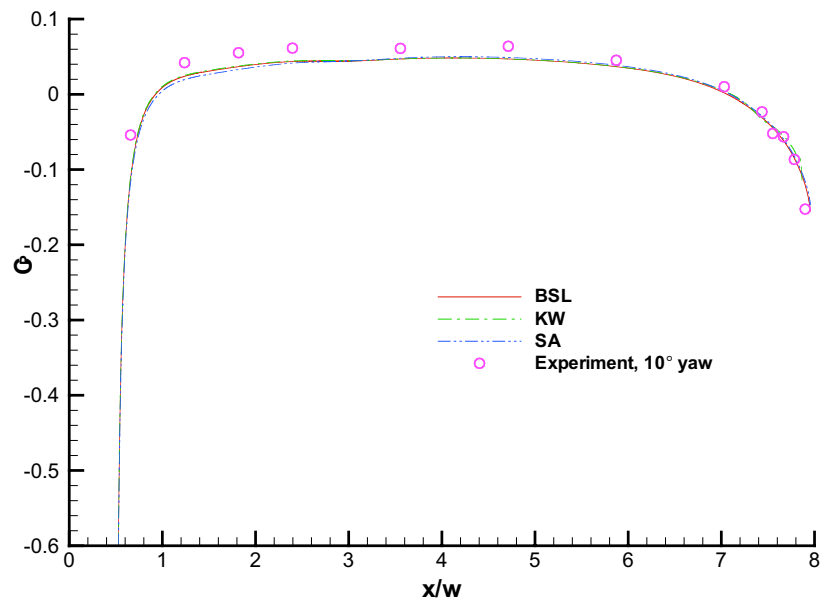


Fig. 45. Comparison of the computed C_p to the NASA experimental data, windward side of GTS, 10° yaw.

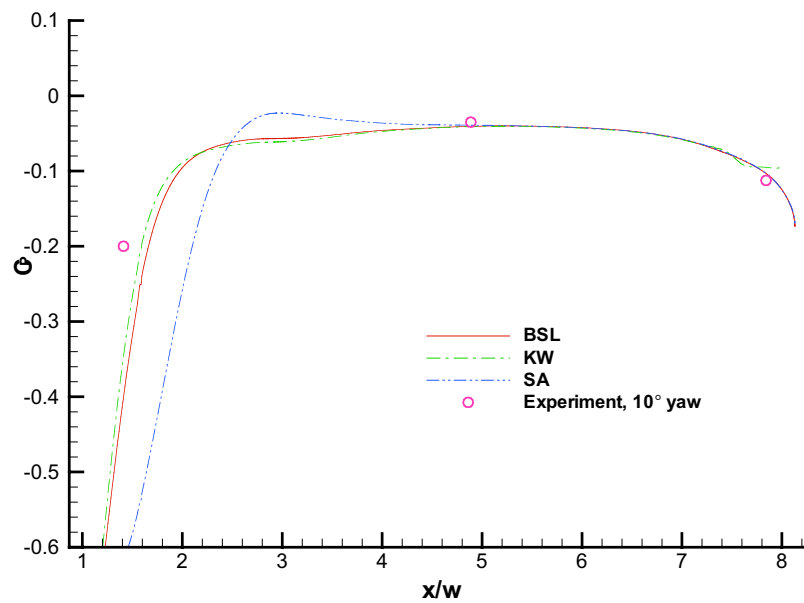


Fig. 46. Comparison of the computed C_p to the NASA experimental data, leeward side of GTS, 10° yaw.

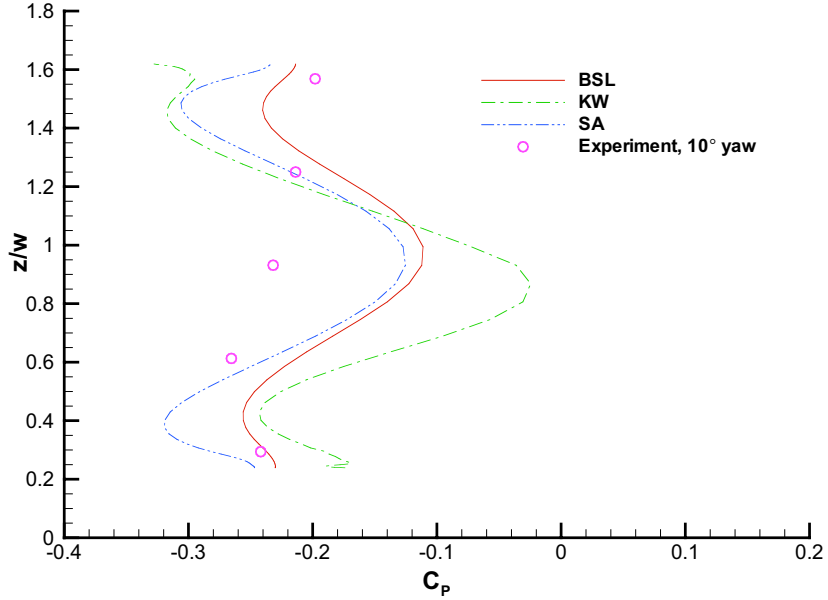


Fig. 47. Comparison of the computed C_p to the NASA experimental data, base of GTS, 10° yaw.

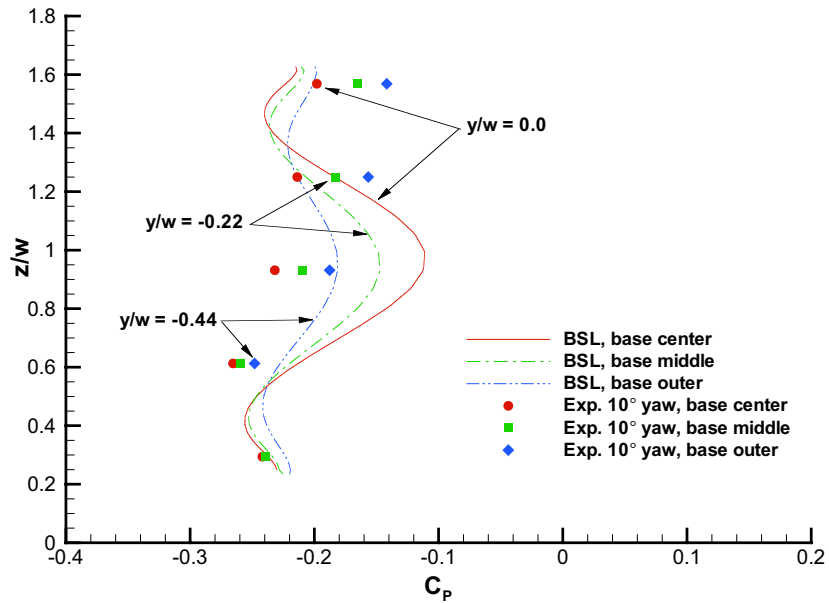


Fig. 48. Comparison of the computed C_p to the NASA experimental data, base of GTS with all pressure taps, 10° yaw.

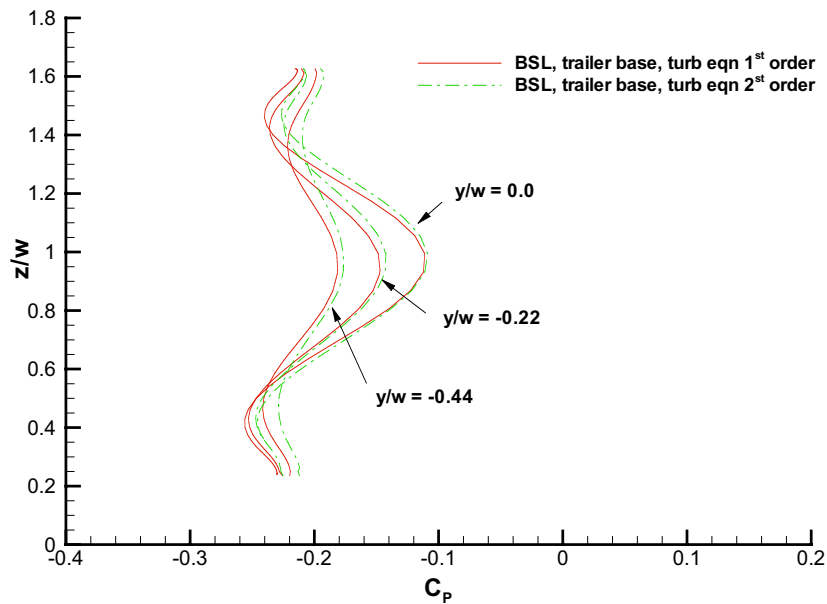


Fig. 49. Discretization order study with BSL turbulence model, base of GTS, 10° yaw.

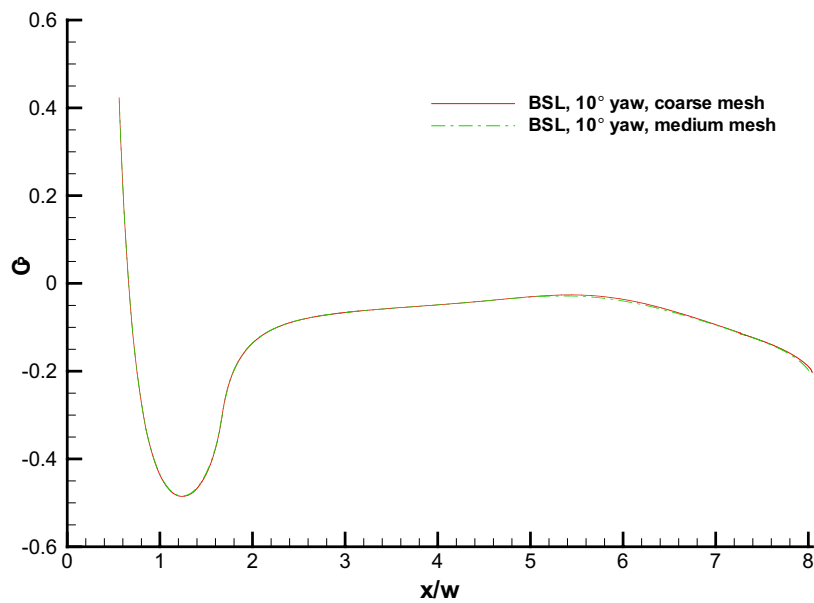


Fig. 50. Grid resolution study with BSL turbulence model, top of GTS, 10° yaw.

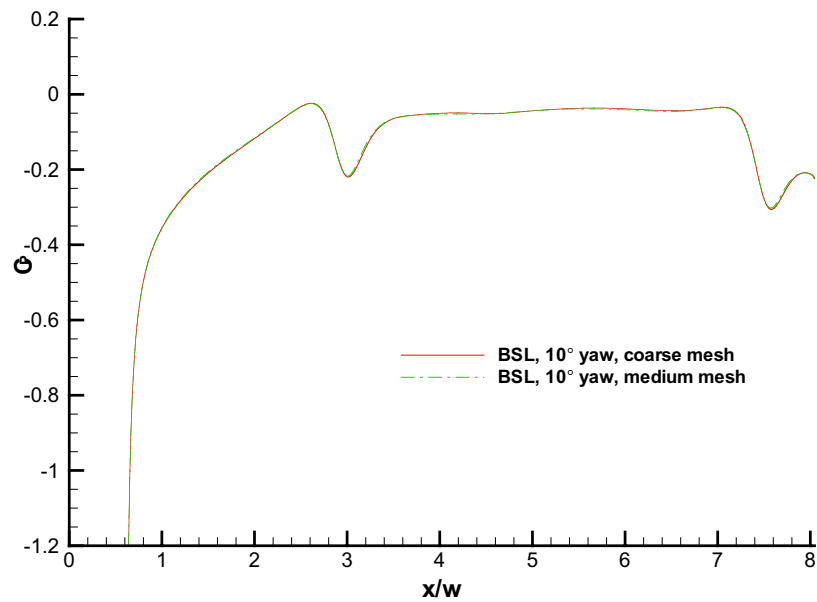


Fig. 51. Grid resolution study with BSL turbulence model, bottom of GTS, 10° yaw.

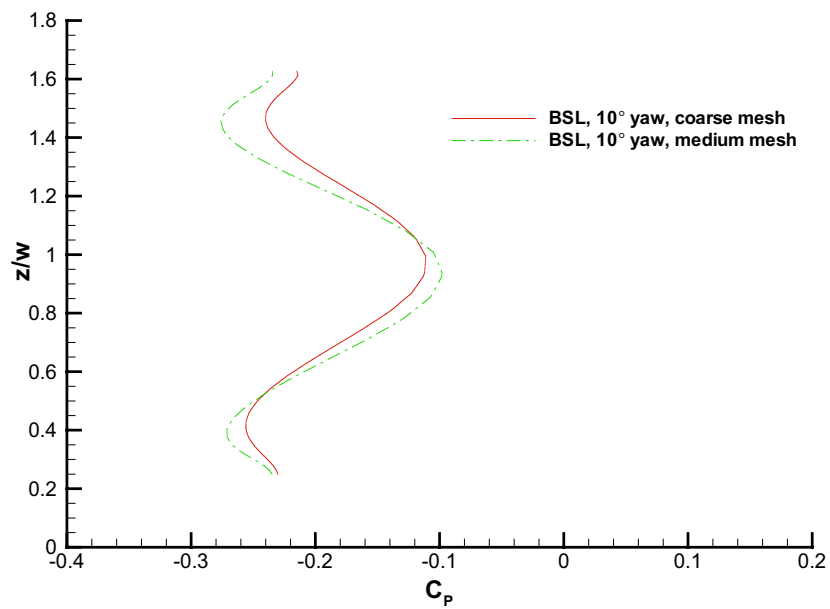


Fig. 52. Grid resolution study with BSL turbulence model, base of GTS, 10° yaw.

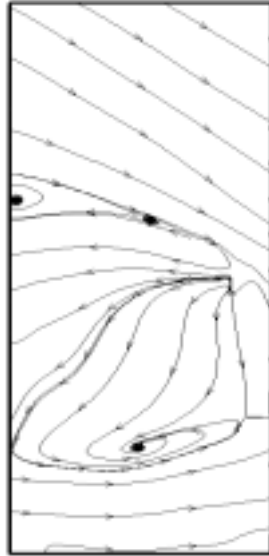


Fig. 53. Time-averaged PIV data, particle traces, horizontal laser sheet located at trailer mid-height, 10° yaw.

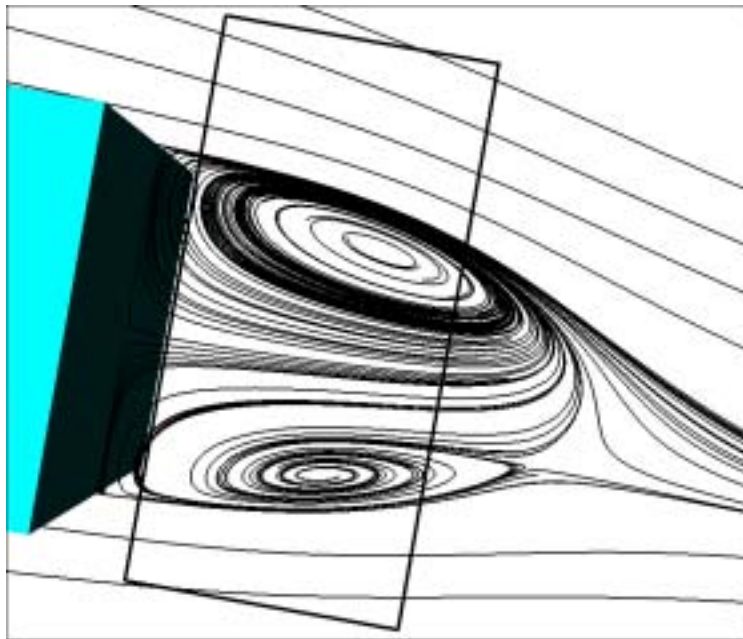


Fig. 54. Particle traces, horizontal cut-plane located at trailer mid-height, BSL solution, 10° yaw.

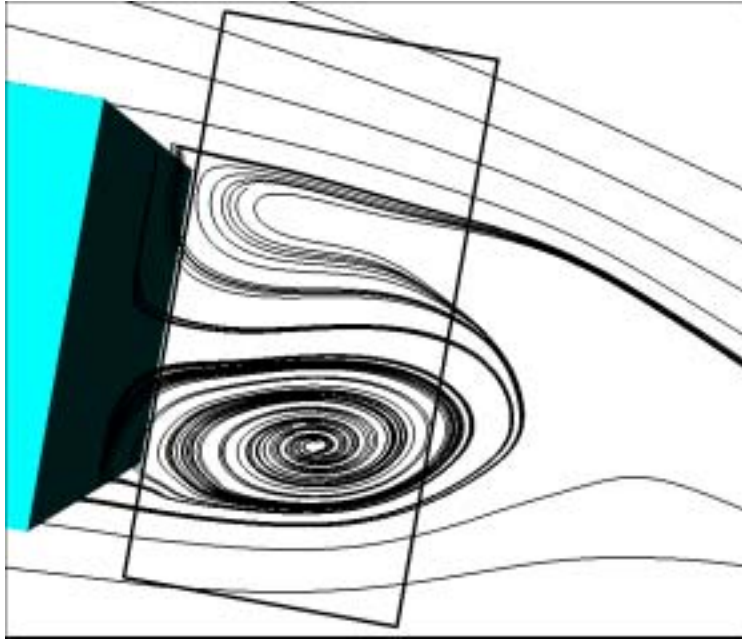


Fig. 55. Particle traces, horizontal cut-plane located at trailer mid-height, KW solution, 10° yaw.

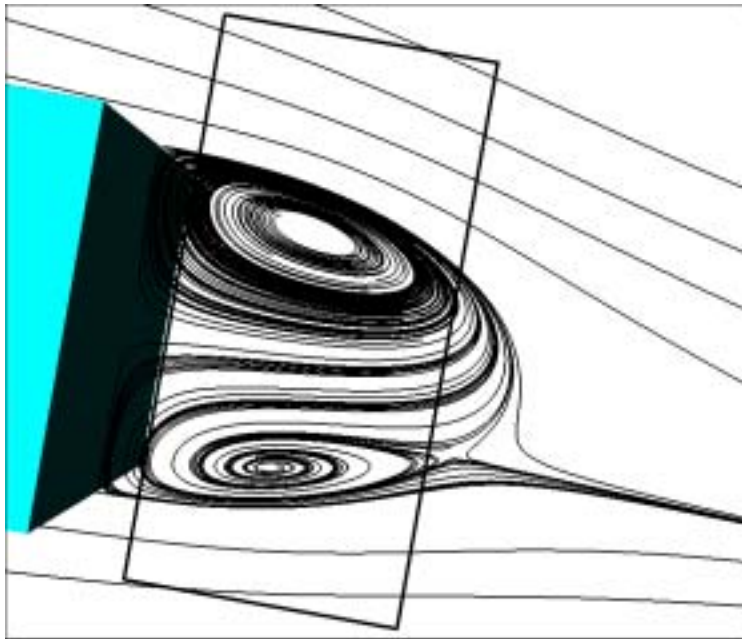


Fig. 56. Particle traces, horizontal cut-plane located at trailer mid-height, the SA solution, 10° yaw.

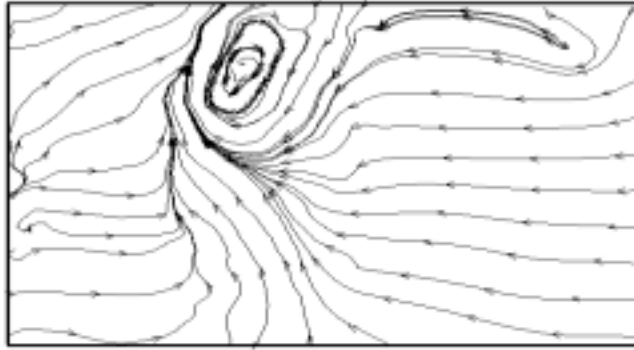


Fig. 57. Time-averaged PIV data, particle traces, $1.14w$ from the trailer base laser sheet, 10° yaw.

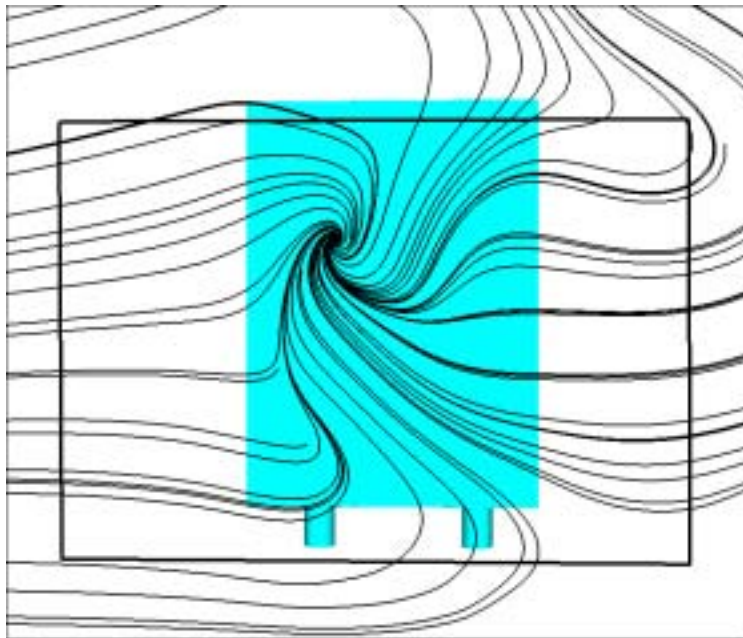


Fig. 58. Particle traces, $1.14w$ from the trailer base laser sheet, BSL solution, 10° yaw.

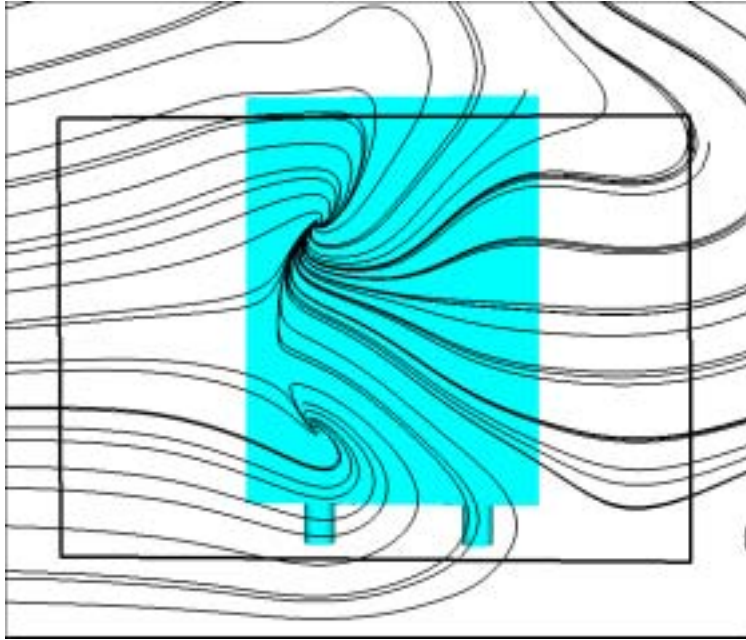


Fig. 59. Particle traces, $1.14w$ from the trailer base laser sheet, KW solution, 10° yaw.

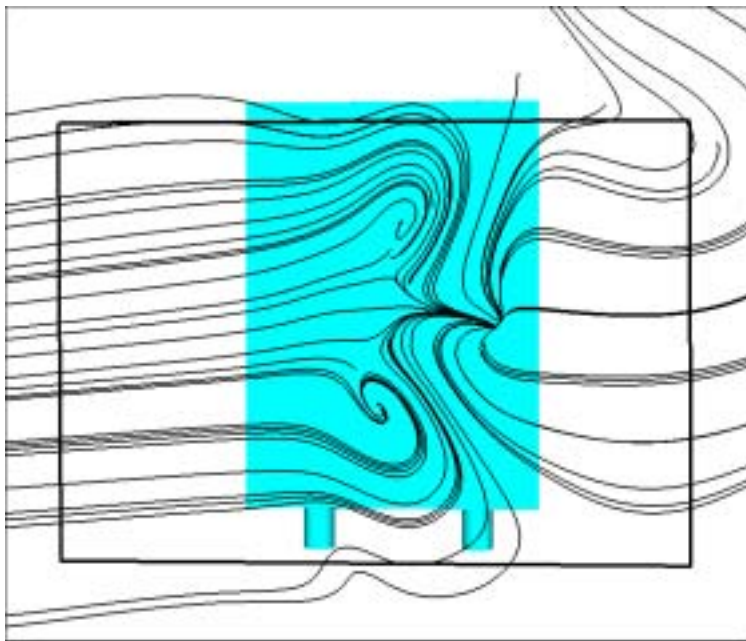


Fig. 60. Particle traces, $1.14w$ from the trailer base laser sheet, SA solution, 10° yaw.

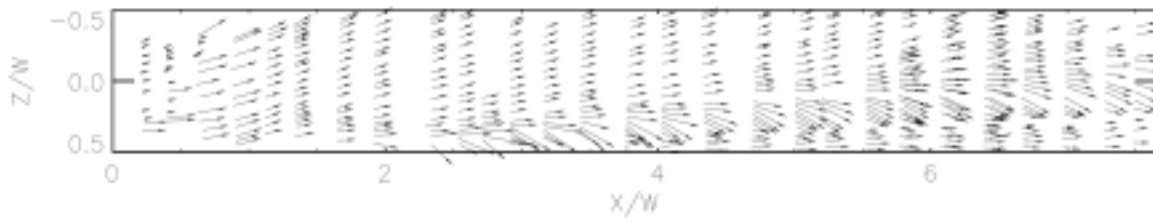


Fig. 61. Oil-Film Interferometry image⁵ showing vortex roll-up on top of truck at 10° yaw.

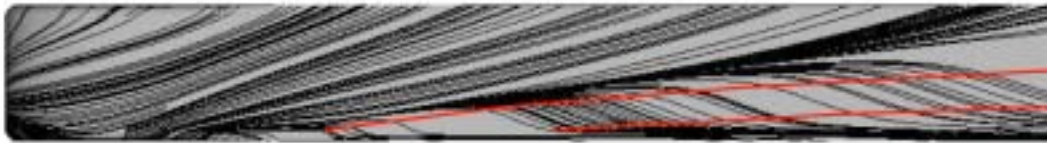


Fig. 62. Comparing the particle traces confined to the top surface of the trailer highlighting the separation and the reattachment lines to the experimental data, BSL solution, 10° yaw.



Fig. 63. Comparing the particle traces confined to the top surface of the trailer highlighting the separation and the reattachment lines to the experimental data, KW solution, 10° yaw.



Fig. 64. Comparing the particle traces confined to the top surface of the trailer highlighting the separation and the reattachment lines to the experimental data, SA solution, 10° yaw.

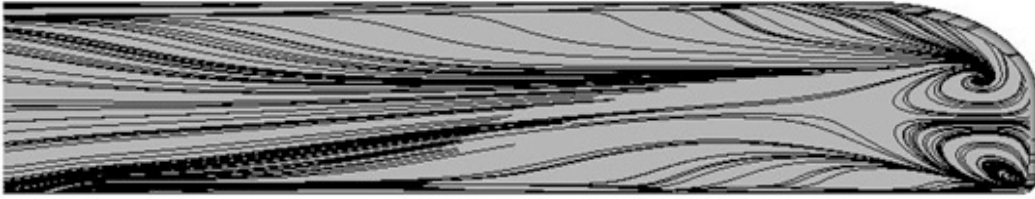


Fig. 65. Particle traces confined to the leeward side of GTS highlighting the separation and the reattachment lines, BSL solution, 10° yaw.

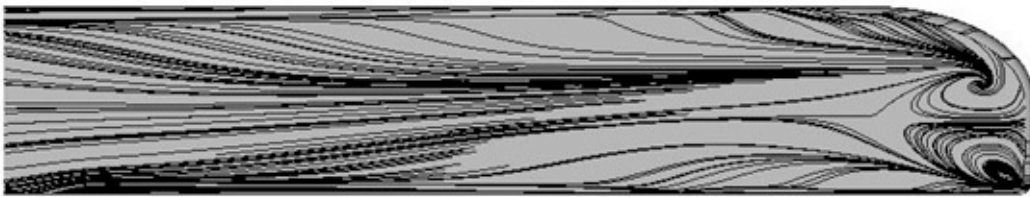


Fig. 66. Particle traces confined to the leeward side of GTS highlighting the separation and the reattachment lines, KW solution, 10° yaw.

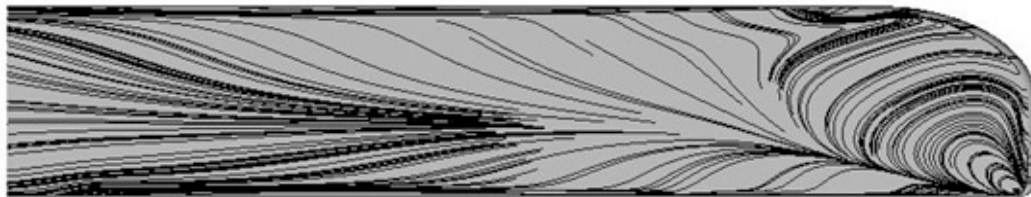


Fig. 67. Particle traces confined to the leeward side of GTS highlighting the separation and the reattachment lines, SA solution, 10° yaw.